Electron Paramagnetic Resonance Studies of Zinc-Substituted Reaction Centers from *Rhodopseudomonas viridis*†

A. T. Gardiner,‡ S. G. Zech, F. MacMillan,§ H. Käss,|| R. Bittl, E. Schlodder, F. Lendzian, and W. Lubitz*

Max-Volmer-Institut für Biophysikalische Chemie und Biochemie, Technische Universität Berlin, Strasse des 17 Juni 135, D-10623 Berlin, Germany

Received March 22, 1999; Revised Manuscript Received June 28, 1999

ABSTRACT: The primary quinone acceptor radical anion $Q_A^{-\bullet}$ (a menaquinone-9) is studied in reaction centers (RCs) of *Rhodopseudomonas viridis* in which the high-spin non-heme Fe^{2+} is replaced by diamagnetic Zn^{2+}. The procedure for the iron substitution, which follows the work of Debus et al. [Debus, R. J., Feher, G., and Okamura, M. Y. (1986) *Biochemistry 25*, 2276−2287], is described. In *Rps. viridis* an exchange rate of the iron of ∼50% ± 10% is achieved. Time-resolved optical spectroscopy shows that the ZnRCs are fully competent in charge separation and that the charge recombination times are similar to those of native RCs. The **g** tensor of $Q_A^{-\bullet}$ in the ZnRCs is determined by a simulation of the EPR at 34 GHz yielding $g_x = 2.00597$ (5), $g_y = 2.00492$ (5), and $g_z = 2.00216$ (5). Comparison with a menaquinone anion radical ($MQ_4^{-\bullet}$) dissolved in 2-propanol identifies $Q_A^{-\bullet}$ as a naphthoquinone and shows that only one tensor component (g_x) is predominantly changed in the RC. This is attributed to interaction with the protein environment. Electron−nuclear double resonance (ENDOR) experiments at 9 GHz reveal a shift of the spin density distribution of $Q_A^{-\bullet}$ in the RC as compared with $MQ_4^{-\bullet}$ in alcoholic solution. This is ascribed to an asymmetry of the Q_A binding site. Furthermore, a hyperfine coupling constant from an exchangeable proton is deduced and assigned to a proton in a hydrogen bond between the quinone oxygen and surrounding amino acid residues. By electron spin−echo envelope modulation (ESEEM) techniques performed on $Q_A^{-\bullet}$ in the ZnRCs, two ^{14}N nuclear quadrupole tensors are determined that arise from the surrounding amino acids. One nitrogen coupling is assigned to a $N^{\delta(1)}$−H of a histidine and the other to a polypeptide backbone N−H by comparison with the nuclear quadrupole couplings of respective model systems. Inspection of the X-ray structure of *Rps. viridis* RCs shows that His(M217) and Ala(M258) are likely candidates for the respective amino acids. The quinone should therefore be bound by two H bonds to the protein that could, however, be of different strength. An asymmetric H-bond situation has also been found for $Q_A^{-\bullet}$ in the RC of *Rhodobacter sphaeroides*. Time-resolved electron paramagnetic resonance (EPR) experiments are performed on the radical pair state $P_{960}^{+\bullet}Q_A^{-\bullet}$ in ZnRCs of *Rps. viridis* that were treated with o-phenanthroline to block electron transfer to Q_B. The orientations of the two radicals in the radical pair obtained from transient EPR and their distance deduced from pulsed EPR (out-of-phase ESEEM) are very similar to the geometry observed for the ground state $P_{960}Q_A$ in the X-ray structure [Lancaster, R., Michel, H. (1997) *Structure* 5, 1339].

In bacterial reaction centers (RCs)[1] the light-induced charge separation starts with the donation of an electron from the lowest excited singlet state of the primary donor P*, a bacteriochlorophyll (BChl) dimer, to an electron transport (ET) chain comprising monomeric BChl, bacteriopheophytin (BPh), and two quinones (*1*, *2*). The quinones act in sequence in the ET process in the RC. They have different redox potentials. The primary quinone, Q_A, accepts only one electron and is not protonated, whereas Q_B exhibits the typical two-electron two-proton chemistry (*3*). The quite different behavior of Q_A and Q_B is traced back to the impact of the protein surrounding. The interactions with specific amino acids, e.g., via hydrogen bonds, are thought to fine-tune the structural and electronic pro-

† This work has been supported by grants from Deutsche Forschungsgemeinschaft (Sfb 312, TP A4/A5), the Alexander von Humboldt-Stiftung (to A.T.G.), NaFöG Berlin (to S.G.Z.), and Fonds der Chemischen Industrie (to W.L.).

* Corresponding author: Phone +49 30 314 21419; Fax +49 30 314 21122; e-mail lubitz@echo.chem.tu-berlin.de.

‡ Present address: Division of Biochemistry and Molecular Biology, Davidson Building, University of Glasgow, Glasgow G12 8QQ, Scotland.

§ Present address: J.W. Goethe-Universität, Marie-Curie-Str. 11, 60439 Frankfurt/M, Germany.

|| Present address: Phys. Chemie III, TH Darmstadt, Petersenstr. 20, 64287 Darmstadt, Germany.

[1] Abbreviations: AAS, atomic absorption spectroscopy; BChl, bacteriochlorophyll; BPh, bacteriopheophytin; CCRP, correlated coupled radical pair; ENDOR, electron−nuclear double resonance; EPR, electron paramagnetic resonance; ESE, electron spin echo; ESEEM, electron spin−echo envelope modulation; ET, electron transfer; FeCy, ferricyanide; hfc, hyperfine coupling constant; LDAO, lauryldimethylamine *N*-oxide; MQ_4, menaquinone-4; mw, microwave; NQR, nuclear quadrupole resonance; Q_A, primary quinone electron acceptor; Q_B, secondary quinone electron acceptor; RC, reaction center; RP, radical pair; RT, room temperature; UQ_{10}, ubiquinone-10; ZnRC, zinc-substituted reaction center.

10.1021/bi990661c CCC: $18.00
Published on Web 08/19/1999

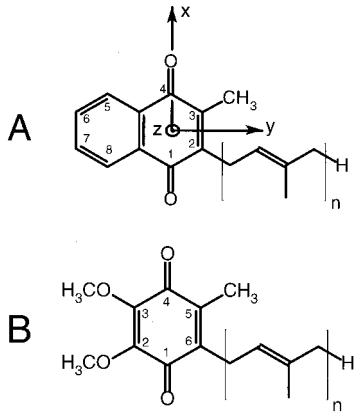

FIGURE 1: Structural formulas and numbering schemes of menaquinone-*n* (A) and ubiquinone *n* (B). *n* denotes the number of isoprenoid units; $n = 9$ for *Rps. viridis* RCs. For MQ the molecular axes are given, which are assumed to coincide with the **g** tensor principal axes (*12*). The protons bound directly to the π-system are called α-protons; protons that are two bonds away from the π-system are called β-protons, e.g., the methyl protons at position 3 of MQ. Protons that are three bonds away are γ-protons, e.g., the CH at the second carbon of the isoprenyl chain of MQ. The quinone oxygens (O_1 and O_4) are labeled according to the C atoms they are bound to.

perties of Q_A and Q_B for optimum function in the RC (*4*).

Information on the geometrical structure of the two quinones and their binding sites can be derived from X-ray crystallography performed on RC single crystals (*5*, *6*). The method of choice to study details of the electronic structure is EPR spectroscopy performed on the radical anions $Q_A^{-\bullet}$ and $Q_B^{-\bullet}$ formed in the ET process (*4*). In native, iron-containing RCs the two quinone radicals are, however, strongly magnetically coupled to the non-heme, high-spin Fe^{2+} and only broad spectra can be obtained at cryogenic temperatures (*7*−*10*). Information about the electronic structure of the semiquinone radical anions in the RC can only be obtained either by removing the Fe^{2+} or by replacing it by another divalent metal like Zn^{2+}, which is diamagnetic. Such a metal exchange has been achieved for the RC of *Rhodobacter sphaeroides* R-26 (*11*) but not for any other photosynthetic bacterium. In *Rb. sphaeroides* both Q_A and Q_B are ubiquinone-10 (UQ_{10}) molecules (see Figure 1).

For *Rb. sphaeroides* R-26 it could be shown by EPR and in particular by electron−nuclear double resonance (ENDOR) that the electron−nuclear hyperfine coupling constants (hfcs) of ^1H, ^{17}O (*13*, *14*), and ^{13}C (*15*, *16*) are different for $Q_A^{-\bullet}$ and for $Q_B^{-\bullet}$. Whereas $Q_B^{-\bullet}$ is quite similar to the free $UQ_{10}^{-\bullet}$ in alcoholic solutions, $Q_A^{-\bullet}$ shows distinctly different hfcs. This was attributed to hydrogen bonds of different strengths between the carbonyl groups of the quinone and the surrounding amino acids. The strength of the H-bonds was deduced from the proton hfcs of the hydrogens in these H-bonds obtained from ENDOR spectroscopy (*4*, *14*). Information on the amino acids involved in the H-bonding was deduced from electron spin echo envelope modulation (ESEEM) spectroscopy applied to $Q_A^{-\bullet}$ and $Q_B^{-\bullet}$. By this technique, ^{14}N nuclear quadrupole coupling constants of the surrounding protein were observed and assigned to specific amino acid residues by comparison with data from the literature (*17*−*19*).

Various publications have appeared that deal with the radical pair (RP) states $P^+Q_A^{-\bullet}$ in ZnRCs of *Rb. sphaeroides*, using transient and pulsed EPR techniques that aimed at the determination of the relative geometrical arrangement and the precise distance of the two radicals in the RP (for a recent review see ref 20). These techniques were also successfully used to investigate light-induced structural changes in RCs that were frozen either in the dark or in the light during illumination (*21*, *22*).

In the RC of *Rhodopseudomonas (Rps.) viridis* the primary donor is a BChl *b*-dimer, called P_{960}, the intermediate acceptors are BChl *b* and BPh *b*, the primary quinone, Q_A, is a menaquinone-9 (MQ_9), and Q_B is a ubiquinone-9 (UQ_9) molecule (see Figure 1). Both quinones are coupled to a high-spin Fe^{2+}. In contrast to *Rb. sphaeroides*, the RC of *Rps. viridis* contains a tightly bound cytochrome subunit with four heme molecules. The RC has been crystallized and a detailed X-ray crystallographic structure is available with 2.45 Å resolution (*5*). So far, a removal and replacement of the high-spin Fe^{2+} has not been reported for this RC. Removal of the iron and replacement with Zn^{2+} would enable the investigation of the semiquinone states by EPR techniques as described above for *Rb. sphaeroides*. This is important not only for a more thorough spectroscopic characterization of the RC of *Rps. viridis* but also for better understanding Nature's basic concept to form the specific quinone binding sites, i.e., binding sites for cofactors with unusual properties in a membrane protein.

Recently, we have reported on the biosynthetic enrichment of Zn in the RC of *Rps. viridis* by growing bacteria on low-iron/high-zinc medium (*23*). This method gave only fairly low yields of Zn incorporation (≈5%). In this paper we report on the replacement of the Fe^{2+} by Zn^{2+} in the RC of *Rps. viridis* by the chemical method introduced by Debus et al. (*11*). The obtained ZnRCs are characterized and the primary quinone radical anion $Q_A^{-\bullet}$ and the radical pair $P_{960}^{+\bullet}Q_A^{-\bullet}$ are investigated by using EPR, ENDOR, ESEEM, and transient/pulsed EPR techniques, respectively.

MATERIALS AND METHODS

Preparation of FeRCs of Rps. viridis. Wild-type Fe-containing *Rps. viridis* RCs were prepared by a protocol developed from ref *24*. Approximately 20 g (wet weight cell paste) of *Rps. viridis* cells were ultrasonicated and the membrane fragments were adjusted to $OD_{1012}^{1cm} = 100$ with 20 mM Tris-HCl, pH 8.0. Lauryldimethylamine *N*-oxide (LDAO) was added dropwise to 1% and stirred for 10 min at room temperature (RT) in the dark. Following ultracentrifugation (50 000 rpm, Beckman 60Ti rotor, 90 min), the supernatant was decanted and retained, whereas the pellet was resuspended and again adjusted to $OD_{1012}^{1cm} = 100$ with 20 mM Tris-HCl, pH 8.0, and the procedure was repeated 3−4 times. Usually, the supernatant from the first extraction could be discarded as it contained no RC/core conjugates, whereas the remaining supernatants were pooled, concentrated, and loaded onto a DE52 (Whatman) column equilibrated with 20 mM Tris-HCl, and 1% LDAO, pH 8.0, and further washed with approximately 1 L of this solution to remove dissociated pigments and denatured polypeptides. The brown, presently impure RC band was then eluted from the column with high-salt buffer, dialyzed, concentrated, and loaded onto a DEAE column equilibrated with 10 mM Tris-HCl, 0.1% LDAO, and 0.1 mM EDTA, pH 8.0 (TLE buffer).

The brown RCs were washed with sufficient TLE until the eluate contained no pigment/denatured protein (gauged by absorption at 280 nm) and then eluted with a salt gradient and dialyzed into the appropriate detergent prior to use. A typical yield from a preparation was around 50 mg of RC from 20 g of cell paste with an optical purity ratio of $A_{280}/A_{830} \approx 2.4$. For further preparation the detergent LDAO was exchanged with sodium cholate (NaChol) following (*11*).

Preparation of ZnRCs of Rps. viridis. Rps. viridis cultured on high-Zn^{2+}/low-Fe^{2+} medium incorporates only approximately 5% Zn^{2+} into the RC (*23*). To obtain a higher zinc enrichment it was necessary to adapt the biochemical procedure used to reversibly dissociate the H-subunit and exchange the non-heme iron developed by Debus et al. (*11*) for *Rb. sphaeroides*. This method has the potential to produce RCs with $\geq$90% Zn^{2+}.

Rps. viridis FeRC ($OD_{832}^{1cm} = 30$) in NaChol were diluted to $OD_{832}^{1cm} = 10$ so that the final buffer solution was 50 mM Tris-HCl and 0.033% NaChol, pH 8.0. The RCs were slowly stirred at 4 °C, *o*-phenanthroline was added (4 mM), and the solution was allowed to equilibrate for 2 min, after which 1.5 M potassium thiocyanate (KSCN) was slowly added. This was incubated at 4 °C for precisely 60 min, after which time the solution was placed into dialysis (four changes over 24 h) against 10 mM Tris-HCl, 0.025% NaChol, and 0.1 mM $ZnCl_2$, pH 7.7, whereupon the buffer was changed (four times over 24 h) to 10 mM Tris-HCl, 0.025% NaChol, and 1 mM ETDA, pH 8.0, to remove any unspecifically bound zinc ions. This procedure results in a fraction of RCs that do not reassemble correctly; i.e., the sample contains a mixture of nonreassociated H and LM subunits in addition to correctly associated ZnRCs. To purify the ZnRC from the nonreassociated subunits the "crude" ZnRC preparation was passed at 4 °C through a column of organomercurial agarose (Affi-Gel 501, Bio-Rad Laboratories). The organomercurial function readily forms a covalent mercaptide bond with free sulfhydryls; therefore, this material has a high capacity for selectively purifying SH-containing proteins. The RCs were loaded onto the column and subsequently washed with 50 mM Tris-HCl, 0.025% NaChol, 0.1% LDAO, and 0.2 M $LiClO_4$, pH 7.7. Under these conditions the LM subunits pass through unbound, whereas the RCs and H subunits are retained on the column. After washing with several column volumes of 50 mM Tris-HCl, 0.025% NaChol, and 0.1% LDAO to remove the $LiClO_4$, the reconstituted ZnRCs were eluted with a cysteine hydrochloride gradient and then dialyzed to yield intact RCs in 10 mM Tris-HCl, 0.025% NaChol, and 0.1 mM EDTA (TCE buffer).

Determination of the Zn^{2+} Content in the Rps. viridis RCs. For the determination of the Zn^{2+} content, two different methods were used: (i) time-resolved measurements of the radical pair state $P_{960}^{+\bullet}Q_A^{-\bullet}$, which are described in detail below, yield information on the relative intensities of $P_{960}^{+\bullet}$ and $Q_A^{-\bullet}$, from which the Zn^{2+} content can be derived, or (ii) atomic absorption spectroscopy measurements. Metal contents were determined with a Varian-Techtron AA-5 spectrometer with an acetylene/air flame or a model 61 carbon rod atomizer. Standard solutions were prepared by diluting 1000 ppm solutions of $FeCl_3$ or $ZnCl_2$ into TCE buffer.

Transient Optical Spectroscopy. Flash-induced absorbance changes were measured with a laboratory-built flash spectrophotometer. The measuring light of a 250 W tungsten lamp (Osram) passed through an interference filter, a 1 cm optical cuvette, and a combination of interference and edge filters in front of the photodiode (OSD 100-5T from Centronic or C30642 from EG&G for measurements at 1250 nm). The photodiode loaded with 1 kΩ was connected to an amplifier (TEK AM 502 from Tektronix). The signals were digitized and averaged by a transient recorder (TDS 410 from Tektronix). The samples were excited by nonsaturating flashes from a Xe lamp of about 15 μs duration filtered by a colored glass (CS96-4 from Corning).

The RC solution was diluted to $OD_{832}^{1cm} = 1$ and 50 μM potassium ferricyanide (FeCy) was added to prevent premature reduction of $P_{960}^{+\bullet}$ by heme 3 in the cytochrome subunit, which is only approximately 50% oxidized. At pH 9.0 and above, $Q_A^{-\bullet}$ is not oxidized by FeCy. When the $P_{960}^{+\bullet}Q_A^{-\bullet}$ charge recombination rate was being measured, 4 mM *o*-phenanthroline was added to inhibit electron transfer to the UQ_9 in the Q_B site. For the measurements of $P_{960}^{+\bullet}Q_B^{-\bullet}$ charge recombination, UQ_9 was added to the RC in 10-fold molar excess in ethanol solution and allowed to diffuse into the protein by stirring overnight at RT. The UQ_9 was bought from Sigma.

Generation of $Q_A^{-\bullet}$ by Dithionite Reduction. Rps. viridis ZnRCs ($OD_{832}^{1cm} = 100$) were dialyzed overnight in anaerobic TCE buffer. A fresh 0.5 M dithionite solution was prepared in 1 M Tris-HCl, 0.025% NaChol, and 0.1 mM EDTA, pH 8.0. The RC solution was transferred under argon to an EPR tube that was being continuously flushed with argon whereupon $^1/_{10}$ volume of dithionite solution was added, mixed, and shock-frozen by immersion in liquid nitrogen. The samples were stored at 77 K. Samples were also prepared by 10-fold dilution of ZnRCs ($OD_{832}^{1cm} = 100$) into D_2O buffer at room temperature for approximately 3 h. The sample was reconcentrated (Centricon) and the procedure was repeated three times. The D_2O-exchanged ZnRCs were reduced as described above with D_2O-based solutions.

Generation of MQ_4 Radical Anion in Solution. The menaquinone-4 anion radical ($MQ_4^{-\bullet}$) was used as model system for $Q_A^{-\bullet}$ in the RC. It was generated by dissolving the quinone (approximately 1 mM) in slightly basic (potassium *tert*-butylate, 10-fold molar excess) anaerobic solutions of either protonated or fully deuterated 2-propanol. The solution was further deoxygenated in the EPR sample capillary by bubbling with purified oxygen-free argon for 2−3 min and then shock-frozen by immersion in liquid nitrogen.

Q-Band EPR Measurements. Q-Band cw EPR (34 GHz) spectra have been recorded on a Bruker ER 200D spectrometer equipped with a Bruker Q-band microwave bridge, Bruker ER5106 QT resonator, and an Oxford CF 935 cryostat. The Q-band EPR powder spectra have been analyzed with a self-written simulation and fit program that is based on the work of Rieger (*25*) using a modified Levenberg−Marquardt nonlinear least-squares model (*26*). This simulation routine includes second-order effects and can deal with an arbitrary number of nuclei with noncollinear g and hf tensors.

Time-Resolved EPR Measurements. All time-resolved EPR experiments were performed on a Bruker ESP 380 E spectrometer as previously described for transient EPR (*27*) and pulsed EPR experiments (*28*). For Q-band experiments we used the Bruker ER 051 QG microwave bridge and a home-built Q-band resonator using the coupling concept of the Bruker 5106 QT resonator. The time resolution of the setup in transient EPR mode was about 50 ns at X-band and 100 ns at Q-band. The transient EPR spectra were extracted from the two-dimensional (time/field) data set as the difference between two time gates, one after and one before the laser flash as described in ref *29*. This removes all contributions from stable radicals in the sample, i.e., signals not initiated by the laser flash. Light excitation was achieved by a Q-switched and frequency-doubled Nd:YAG laser (Spectra Physics GCR 130, $\lambda = 532$ nm, 8 ns pulse width, ≤ 5 mJ/pulse incident to the sample).

About 40 μL of the sample ($OD_{832}^{1cm} = 90$) was filled into a quartz tube with 2 mm inner diameter and 3 mm outer diameter and frozen in the dark in liquid nitrogen. For detection of the transient Q-band spectrum of $P_{960}^{+}\bullet Q_A^{-}\bullet$, an oxidation of the cytochrome hemes was achieved by addition of a 80-fold excess of a 1:9 (v/v) solution of $K_4Fe(CN)_6/K_3[Fe(CN)_6]$ (FeCy) before the sample was frozen (*30*) (see below for further details).

ESEEM and ENDOR Spectroscopy. The stimulated echo (three-pulse) ESEEM experiments on $Q_A^{-}\bullet$ were also obtained on the Bruker ESP 380 E spectrometer. Two-dimensional experiments were performed in order to get the complete spectral information. The subtraction of the relaxation decay and the evaluation of the time domain spectra were done with the ESP 380 software as described in detail in ref *31*.

The out-of-phase ESEEM measurements of the RP state $P_{960}^{+}\bullet Q_A^{-}\bullet$ were carried out as described earlier (*28*). Here we used a $\zeta/2-\zeta$ pulse sequence with $\zeta \approx 130°$ (*21*). The magnetic field was set to the center of the transient EPR spectrum.

^{1}H-ENDOR spectra of $Q_A^{-}\bullet$ and $MQ_4^{-}\bullet$ were recorded on a Bruker ESP 300 E spectrometer with a self-built ENDOR/TRIPLE extension (*32*, *33*) and a TM_{110} ENDOR cavity of local design (*34*). The temperature was controlled either with a Bruker ER 4111 VT nitrogen gas flow unit or with an Oxford 910 helium cryostat.

RESULTS AND DISCUSSION

Characterization of the ZnRCs

Preparation of ZnRC of Rps. viridis. To obtain chemically exchanged *Rps. viridis* ZnRCs, FeRCs were prepared and treated with KSCN to dissociate the H subunit and with *o*-phenanthroline to chemically exchange the non-heme iron with Zn^{2+}. Native (panel A) and Coomassie-stained SDS−PAGE gels (panel B) of this procedure are presented in Figure 2. In panel A, lane 1, the Fe-containing RCs that undergo the procedure are shown. Lane 2 illustrates the effect of the KSCN treatment in that the nonpigmented H subunit is dissociated to form the LM subunit, which migrates more slowly than the native RC. Lanes 3 and 4 show the preparation after Affi-Gel chromatography: lane 3 is the column eluate containing the LM complex, whereas lane 4 is the putative Zn-containing RC, which is eluted from the column with the cysteine solution. It can be seen clearly that the H subunit has reassociated correctly to form the intact RC complex. This has been confirmed in panel B, where the same samples were loaded onto a SDS−PAGE gel and stained with Coomassie blue. Lane 1 is FeRC and all four subunits of the complex are visible. In lane 2 the H-subunit has been dissociated from LM but is still present in the sample; however, after Affi-Gel treatment, the column eluate in lane 3 clearly contains only LM with the H subunit no longer present. Lane 4 is the Zn-containing RC sample, which was used for the subsequent experiments and clearly consists of intact RCs with all four subunits. We have also tried to prepare iron-free RCs by a similar procedure as described above, without success. Presumably, the preparation is not very stable.

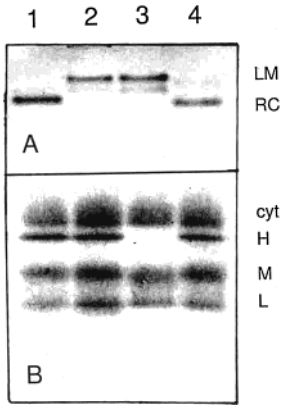

FIGURE 2: Native and SDS−PAGE gels showing the preparation of *Rps. viridis* ZnRCs. Lane 1, FeRC; lane 2, FeRC treated with KSCN; lane 3, LM complex eluate from Affi-Gel column; lane 4, putative ZnRC eluted from Affi-Gel column. Panel A, unstained, native 5% PAGE gel; panel B, the same samples loaded onto a 15% SDS−PAGE gel and stained with Coomassie blue. For further details see text.

The typical absorption spectrum of intact ZnRCs obtained from our procedure was identical to that of wild-type FeRCs. However, the overall yield obtained (given as the amount of ZnRCs recovered from the Affi-Gel column against the amount of FeRCs at the beginning of the procedure) is approximately 10%; this compares with approximately 80% reported for *Rb. sphaeroides* (*11*). Furthermore, the amount of Zn^{2+} incorporated is also substantially less: $50\% \pm 10\%$ as against 90% for *Rb. sphaeroides* (see below). A possible reason is that the reaction conditions used are not ideal for *Rps. viridis*. A systematic optimization of the various parameters might lead to a better preparation with enhanced Zn^{2+} content and yield.

Determination of Zn^{2+} Content in ZnRCs. The amount of Zn^{2+} substitution can be checked, in principle, by atomic absorption spectroscopy (AAS), mass spectrometry, or standard (cw) EPR methods. These methods are, however, not able to determine *directly* the Zn^{2+} replacing the non-heme iron ion. EPR spectroscopy determines the amount of $Q_A^{-}\bullet$ decoupled from the Fe^{2+}. The detection by AAS is difficult and additionally complicated for *Rps. viridis* RCs because of the bound cytochrome, which contains four iron ions.

Figure 3 shows the time-resolved Q-band EPR-spectra of $P_{960}^{+}\bullet$ and $Q_A^{-}\bullet$ recorded at low microwave powers, i.e.,

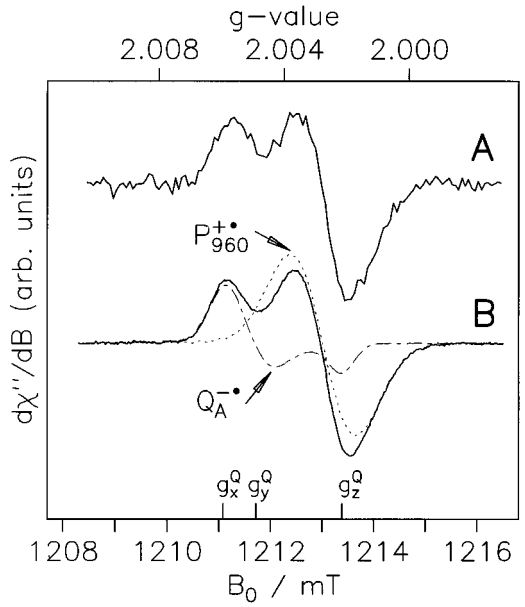

FIGURE 3: (A) Time-resolved Q-band spectrum of $P_{960}^{+\bullet}Q_A^{-\bullet}$ integrated 1.2−5.0 ms after the initial laser flash. The spectrum has been measured by field modulation and lock-in detection (ν = 34.0 GHz). (B) Cw spectra of $P_{960}^{+\bullet}$ (- - -) and $Q_A^{-\bullet}$ (− - −) and weighted sum (—) if 50% uncoupled $Q_A^{-\bullet}$ is assumed.

under nonsaturating conditions for both radicals. According to the late integration window (5−10 ms after the laser flash), the spectra show a superposition of the signals of $P_{960}^{+\bullet}$ and $Q_A^{-\bullet}$ in thermal equilibrium (see Figure 3B). As can be seen, the g_x and g_y components of the g tensor of $Q_A^{-\bullet}$ (not resolved at Q-band) are separated from the $P_{960}^{+\bullet}$ signal at $g = 2.0026$ (1), while the g_z component overlaps with the EPR line of $P_{960}^{+\bullet}$ (see below and Table 2 for details).

The superposition of the steady-state cw spectra from $P_{960}^{+\bullet}$ and $Q_A^{-\bullet}$ obtained in separate samples from either FeCy-treated ($P_{960}^{+\bullet}$) or $Na_2S_2O_4$-treated ($Q_A^{-\bullet}$) ZnRCs of *Rps. viridis* (Figure 3B) closely resemble the experimental spectrum of the radical pair shown in Figure 3A. From this superposition the amount of decoupled $Q_A^{-\bullet}$ can be calculated by double-integration of both cospectra and by comparing the relative intensities of the $Q_A^{-\bullet}$ and the $P_{960}^{+\bullet}$ signals. From this calculation we conclude that the amount of decoupled $Q_A^{-\bullet}$ and thus the degree of Zn^{2+} substitution is about 50% ± 10%.

The AAS measurements suggested that the degree of Zn^{2+} is of the order of 20%. However, due to the fact that AAS measurements are inherently more difficult with *Rps. viridis* RCs than *Rb. sphaeroides* (see above), we feel that the higher figure derived from the EPR is more accurate. In principle, some of the RCs could contain no metal. However, optical recombination kinetics experiments indicate that essentially no metal-free RCs are present in our samples (see below).

Charge Recombination Kinetics in Rps. viridis ZnRCs. The kinetics of charge recombination between $P_{960}^{+\bullet}$ and $Q_A^{-\bullet}$ or $Q_B^{-\bullet}$ were measured to establish whether the reversible dissociation and reassociation of the H subunit by chaotropic agents resulted in a functional RC. Figure 4 compares the charge recombination of $P_{960}^{+\bullet}Q_A^{-\bullet}$ (left) and of $P_{960}^{+\bullet}Q_B^{-\bullet}$ (right) in native FeRCs and ZnRCs. The formation and decay of the charge-separated states were monitored by measuring the flash-induced absorption changes at 980 nm. The decay kinetics of $P_{960}^{+\bullet}Q_A^{-\bullet}$, measured in the presence of 4 mM

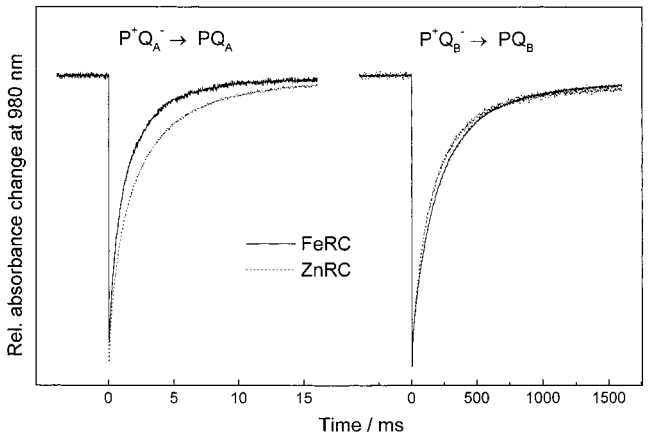

FIGURE 4: Comparison of room-temperature charge recombination kinetics in *Rps. viridis* FeRC and ZnRCs solubilized in LDAO. Flash-induced absorbance changes were monitored at 980 nm. The decay curves are fitted by the sum of two exponentials with lifetimes and relative amplitudes given in Table 1. Conditions: 20 mM Bis-Tris propane (pH 9.0), 100 mM NaCl, 0.1% LDAO, and 50 mM FeCy. The differences between conditions used for Q_A and Q_B are described in the Materials and Methods section.

o-phenanthroline, and of $P_{960}^{+\bullet}Q_B^{-\bullet}$, measured after addition of UQ_9, could be fitted well with the sum of two exponentials. The time constants and relative amplitudes are summarized in Table 1. Our native FeRCs solubilized in LDAO exhibit biphasic recombination kinetics of $P_{960}^{+\bullet}Q_A^{-\bullet}$ and of $P_{960}^{+\bullet}Q_B^{-\bullet}$ that are almost identical to those previously published (*35*, *36*). In ZnRCs containing approximately 50% Zn^{2+} similar recombination kinetics were found. The recombination of $P_{960}^{+\bullet}Q_A^{-\bullet}$ was slightly slower (by about a factor of 1.6) compared to FeRCs (see Figure 4 and Table 1), whereas the recombination kinetics of $P_{960}^{+\bullet}Q_B^{-\bullet}$ were essentially the same in FeRCs and ZnRCs. Little or no effect on the recombination reactions were observed when the RCs were solubilized in NaChol instead of LDAO (see Table 1). This is important since Q_A cannot be reduced by dithionite in LDAO-solubilized RCs to form $Q_A^{-\bullet}$.

It has already been established that Zn-reconstituted RCs from *Rb. sphaeroides*, containing approximately 90% Zn^{2+}, exhibit electron transfer kinetics that are essentially the same as those of native RCs (*11*, *37*, *38*). The small changes in the charge recombination rates observed in our work between ZnRCs and FeRCs from *Rps. viridis* are in agreement with these results. From the work with RCs from *Rb. sphaeroides* it is also known that the removal of Fe^{2+} and/or the H subunit strongly affects the charge recombination rates (*11*, *39*). Especially the recombination of $P_{865}^{+\bullet}Q_B^{-\bullet}$ is significantly slower. If one assumes that these findings also hold for RCs from *Rps. viridis*, our observation that the recombination kinetics of $P_{960}^{+\bullet}Q_B^{-\bullet}$ were essentially the same in our ZnRCs and native FeRCs indicate that the ZnRCs show very little contamination with RCs containing no divalent metal ion or with particles lacking the H subunit.

Experiments on the Anion Radical $Q_A^{-\bullet}$ in ZnRCs

*Determination of the **g**-Tensor Principal Values of $Q_A^{-\bullet}$ in ZnRCs of Rps. viridis.* The Q-band EPR spectra of $Q_A^{-\bullet}$ in *Rps. viridis* ZnRCs and the respective model system $MQ_4^{-\bullet}$ in frozen 2-propanol are presented in Figure 5. The principal **g**-tensor values were obtained from simulations and

Table 1: Flash-Induced Recombination Kinetics for *Rps. viridis* RCs

RC type	detergent	k_{fast}^{-1} [a] (ms)	A_{fast} [b] (%)	k_{slow}^{-1} [a] (ms)	A_{slow} [b] (%)	A_{nd} [c] (%)	ref
			$P_{960}^{+}\bullet Q_A^{-}\bullet \rightarrow P_{960}Q_A$				
FeRC	LDAO	0.66	50.5	2.68	47.8	1.7	this work
	NaChol	0.61	59.4	2.60	39.6	1.0	this work
ZnRC	LDAO	0.99	50.7	4.50	47.4	1.9	this work
	NaChol	1.27	56.4	5.34	42.2	1.4	this work
FeRC	LDAO	0.71	35	2.86	65	0	*35*
		0.80	33.7	3.03	62.5	3.8	*36*
			$P_{960}^{+}\bullet Q_B^{-}\bullet \rightarrow P_{960}Q_B$				
FeRC	LDAO	121	44.9	366	51.9	3.2	this work
	NaChol	102	31.8	375	65.5	2.7	this work
ZnRC	LDAO	102	51.8	350	44.1	4.1	this work
	NaChol	88	42.6	348	54.8	2.6	this work
FeRC	LDAO	88	33	363	61.5	5.5	*36*

[a] k = rate constant. [b] A = amplitude. [c] nd = nondecaying component.

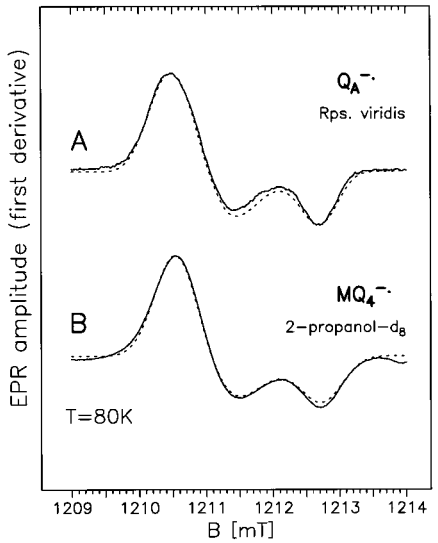

FIGURE 5: Experimental (—) and simulated (- - -) Q-band EPR spectra at 34 GHz of $Q_A^{-}\bullet$ in *Rps. viridis* ZnRC (dithionite reduction) (A) and of the MQ_4 anion radicals in frozen 2-propanol-d_8 (B) at $T = 80$ K. The dotted lines show the computer simulations with the **g** tensor values given in Table 2 and component line widths of 0.19 mT ($Q_A^{-}\bullet$) and 0.25 mT ($MQ_4^{-}\bullet$).

are given in Table 2 along with the corresponding values for $Q_A^{-}\bullet$ in *Rb. sphaeroides* ZnRCs and $UQ_{10}^{-}\bullet$ in 2-propanol (*40*). It is apparent that for $Q_A^{-}\bullet$ in *Rps. viridis* RCs the **g** anisotropy and the isotropic g value $g_{iso} = {}^1/_3\mathrm{Tr}\{\mathbf{g}\}$ are smaller than for $Q_A^{-}\bullet$ in *Rb. sphaeroides* RCs. The principal g-values for the respective model compounds, $MQ_4^{-}\bullet$ and $UQ_{10}^{-}\bullet$ in frozen 2-propanol, show a similar difference. The smaller g_{iso} value in naphthoquinones is the result of a larger delocalization of the spin in the naphthoquinone as compared with the benzoquinone radical. This reduces the spin density on the carbonyl oxygens, which determines the magnitude of the **g** tensor (*12*).

Comparison of the **g** components of $Q_A^{-}\bullet$ in *Rps. viridis* ZnRCs and $MQ_4^{-}\bullet$ in frozen alcohol shows a difference for the g_x values. The same effect has been observed for $Q_A^{-}\bullet$ in ZnRCs of *Rb. sphaeroides* and $UQ_{10}^{-}\bullet$ (*4*, *12*, *40*) (see Table 2). A much larger difference in the g_x values was observed for ubiquinone anion radicals dissolved in alcoholic and etheral solvents (*41*). This was attributed to the formation of H bonds to the carbonyl groups of the quinone in alcoholic solvents that are not present in dry ethers. From the similarities between the **g**-tensor values of $Q_A^{-}\bullet$ in vivo and the model system in alcoholic solution, one can conclude that H bonds to the CO groups of the quinones are present in both environments (*4*, *12*). The observed slight increase of the g_x value of $Q_A^{-}\bullet$ could be explained as a result of a difference in the polarity of the surrounding of the quinones in solution and in the hydrophobic protein pocket (*5*). Furthermore, it could be due to an asymmetry of the H bonds to the carbonyl oxygens in the protein as suggested by various spectroscopic studies on isotopically labeled $Q_A^{-}\bullet$ in *Rb. sphaeroides* (*15*, *16*, *42*−*44*). This view is supported by the recent X-ray structure analysis of *Rps. viridis* RC single crystals (*5*). In the original structure (Brookhaven Protein Data Bank entry 1PRC) (*45*) the distances from the proximal carbonyl oxygen (O_4, closest to the Fe^{2+}) to the nitrogen $N^{\delta(1)}$ of His M217 and the distal carbonyl oxygen (O_1) to the backbone nitrogen of Ala M258 were given as equidistant (3.1 Å). In the improved RC structure (Brookhaven Protein Data Bank entry 2PRC) (*5*) these distances are different, i.e., 2.9 and 3.1 Å, respectively (see Figure 6).

Electron Spin Echo Envelope Modulation of $Q_A^{-}\bullet$ in ZnRCs of Rps. viridis. ESEEM spectroscopy is used to probe the surroundings of $Q_A^{-}\bullet$ in the *Rps. viridis* ZnRC with respect to nitrogen in the vicinity of the menaquinone. For ^{14}N nuclei ($I = 1$), sharp lines from the three zero-field nuclear quadrupole resonance (NQR) transitions can be observed in ESEEM spectra (*48*, *49*), when the so-called cancellation condition is fulfilled; i.e., $|\nu_n - |A|/2| < 2K/3$ (*50*). Then, the hfc and nuclear Zeeman term cancel each other in one m_s state and the three NQR transitions ν_+, ν_-, and ν_0 are observed that are related to the quadrupole parameters by $K = (\nu_- + \nu_+)/6$ and $\eta = 3\nu_0(\nu_- + \nu_+)$ (*48*, *49*). Here $K = e^2qQ/4h$ and $\eta = (q_x - q_y)/q_z$, in which Q is the nuclear quadrupole moment and q is the electric field gradient with principal components q_i ($i = x, y, z$). In the other m_s state a double quantum transition, ν_{dq}, is observed from which the effective hfc can be calculated (*48*, *49*).

In Figure 7 the ESEEM spectrum of $Q_A^{-}\bullet$ is shown. Two sets of corresponding NQR transitions—marked × and ◇—could be assigned in the spectrum to two different ^{14}N nuclei. The resulting NQR coupling constants, K, and asymmetry parameters, η, are collected in Table 3.

From the measured NQR parameters of an ^{14}N nucleus, an identification of amino acid residues binding to $Q_A^{-}\bullet$ is possible (*17*). On the basis of the X-ray structure analysis, likely candidates are His(M217) and Ala(M258); see Figure

Table 2: Comparison of the Principal Values of the Electronic **g** Tensors of $Q_A^{-\bullet}$ in ZnRCs of *Rps. viridis* and *Rb. sphaeroides* and the Respective Model Compounds[a]

quinone	g_x	g_y	g_z	g_{iso}	ref
$Q_A^{-\bullet}$, *Rps. viridis*[b]	2.00597 (5)	2.00492 (5)	2.00216 (5)	2.00435 (5)	this work
$MQ_4^{-\bullet}$ in 2-propanol-d_8	2.00579 (5)	2.00498 (5)	2.00218 (5)	2.00432 (5)	this work
$Q_A^{-\bullet}$, *Rb. sphaeroides*	2.00649 (5)	2.00532 (5)	2.00210 (5)	2.00464 (5)	*40*
$UQ_{10}^{-\bullet}$ in 2-propanol-d_8	2.00632 (5)	2.00533 (5)	2.00215 (5)	2.00460 (5)	*40*

[a] All values from simulations of Q-band EPR spectra; numbers in parentheses are the errors in the last digit. [b] In W-band we obtained $g_x = 2.00599$, $g_y = 2.00494$, $g_z = 2.0220$ (Vrieze *et al.*, unpublished results).

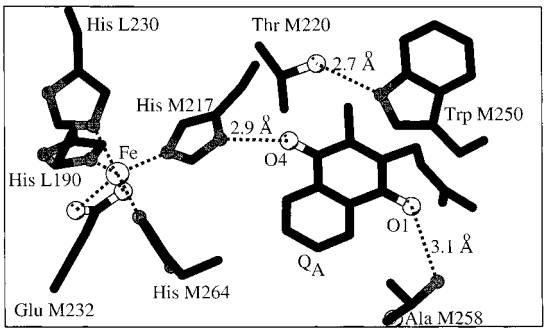

FIGURE 6: Binding sites of the non-heme iron and Q_A in the RC of *Rps. viridis*. Carbon atoms are shown in black, nitrogen atoms in dark gray, oxygen atoms in light gray, and the iron in white. Iron−protein interactions and hydrogen bonds are shown as dashed lines. The distances between the donor and acceptor of the respective hydrogen bonds are indicated. For histidine M217 the ring nitrogen ϵ is ligated to the iron and the nitrogen $\delta(1)$ forms a H-bond to oxygen O_4 of the quinone. This figure was drawn with the program BobScript (*46*), an extension of MolScript (*47*), using the Brookhaven Protein Data Bank coordinate file 2PRC (*5*).

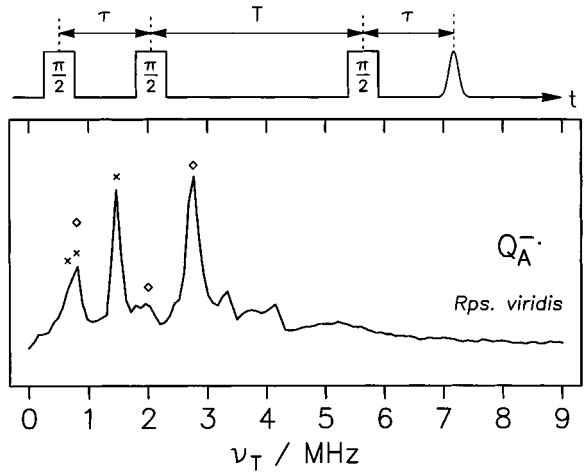

FIGURE 7: Three-pulse (stimulated echo) ESEEM spectra (projections of full 2D data set after Fourier transformation onto the *T* axis) of $Q_A^{-\bullet}$ in *Rps. viridis* ZnRCs. Corresponding sets of zero-field NQR transitions are indicated by symbols (x, ◇). Experimental conditions: temperature 15 K, $T \times t = 512 \times 128$ points. Start values: $T_0 = 200$ ns, $t_0 = 120$ ns. Increments: $\Delta T = 24$ ns, $\Delta t = 8$ ns, $\pi/2$ pulse = 16 ns. A four-phase cycle was employed. Total accumulation time was approximately 3 h. Top: Three-pulse sequence used in the experiment.

6. Alanine contains one amino nitrogen in the peptide bond, whereas in histidine there are additional nitrogen atoms present in the imidazole ring. Published *K* and η values of the imidazole nitrogens in histidine and of typical peptide-bond nitrogens in triglycine and polyglycine are given in Table 3. A comparison with the NQR data of the ^{14}N nuclei determined in this work shows that the evaluated *K* values of 0.80 and 0.41 and η values of 0.52 and 0.69 can be assigned to a peptide nitrogen and to a $N^{\delta(1)}$ from a histidine ligand, respectively. A quite similar result was deduced from ESEEM investigations of the ubiquinone radical anion $Q_A^{-\bullet}$ in *Rb. sphaeroides* R-26 (*17*−*19*) and of the plastoquinone radical anion, $Q_A^{-\bullet}$, in plant photosystem II (*51*, *55*−*57*); see Table 3.[2]

Table 3: Assignment of ^{14}N ESEEM NQR Parameters *K* and η of $Q_A^{-\bullet}$ in ZnRCs of *Rps. viridis* to Histidine or Peptide Nitrogens and Comparison with Literature Values

(A) Experimentally Determined NQR Parameters

quinone	putative bond assignment[a]	*K*	η	ref
$Q_A^{-\bullet}$, *Rps. viridis* ×[b]	His $N^{\delta(1)}$−H	0.41	0.69	this work
$Q_A^{-\bullet}$, *Rps. viridis* ◇	peptide N	0.80	0.52	this work
$Q_A^{-\bullet}$, *Rb. sphaeroides*	His $N^{\delta(1)}$−H	0.41	0.73	*18*
$Q_A^{-\bullet}$, *Rb. sphaeroides*	peptide N	0.76	0.54	*18*
$Q_A^{-\bullet}$, photosystem II	His $N^{\delta(1)}$−H	0.39	0.69	*51*
$Q_A^{-\bullet}$, photosystem II	peptide N	0.82	0.52	*51*, *57*

(B) NQR Parameters for Histidine and Peptide Linkages

compound	bond[a]	*K*	η	ref
histidine	$N^{\delta(1)}$−H	0.36	0.91	*53*
	$N^{\epsilon(2)}$	0.84	0.13	*53*
polyglycine	$N^{(n+1)}$−H	0.77	0.76	*54*
triglycine	$N^{(2)}$−H	0.75	0.48	*54*
	$N^{(3)}$−H	0.77	0.76	*54*

[a] For nomenclature see ref *52*. [b] The symbols × and ◇ refer to the assignment in Figure 7.

It can be concluded that one of the carbonyl oxygens of $Q_A^{-\bullet}$ in *Rps. viridis* is coupled to His(M217). It is reasonable to assign the detected peptide nitrogen to Ala(M258), which most likely takes part in a second H bond to the other carbonyl oxygen of $Q_A^{-\bullet}$. This is in agreement with structural data from the recent X-ray crystallographic study of *Rps. viridis* RCs (Figure 6). Analysis of the double quantum transitions (Figure 7) provides a rough estimate of the hyperfine couplings of the nitrogen nuclei. This yields a value on the order of $2\nu(^{14}N) \approx 2$ MHz that is much larger than the dipolar coupling of about 0.2 MHz that can be estimated for point dipoles separated by a distance of ∼3 Å. Thus, a significant delocalization of the unpaired electron on the quinone to both amino acid residues must take place. Such a transfer of spin density probably involves the hydrogen bonds and could either be by direct overlap or by spin polarization as postulated earlier by Lendzian et al. (*18*) and by Deligiannakis et al. (*55*). Density functional theory (DFT) calculations of hydrogen-bonded quinone radical anions show that such transfer of spin density to the H-bond donor indeed takes place (*59*).

[2] Peloquin et al. (*58*) have recently assigned NQR parameters measured for $Q_A^{-\bullet}$ in photosystem II to a backbone NH (probably of alanine) and to another unassigned peptide nitrogen.

ENDOR of Menaquinone Anion Radical. For an interpretation of the ENDOR spectrum of $Q_A^{-\bullet}$ in *Rps. viridis* ZnRCs, an understanding of the electronic structure of a menaquinone model anion radical is indispensable. Since it is known that the length of the isoprenoid chain does not influence the spin density distribution, we have chosen to investigate $MQ_4^{-\bullet}$ dissolved in 2-propanol as a model system.

For the quinone radical anion in solution, ENDOR lines are expected to occur in pairs symmetrically displayed about the Larmor frequency, ν_n, of the respective nucleus (for $|A| < 2\nu_n$) (*60*):

$$\nu_{\mathrm{ENDOR}}^{\pm} = |\nu_n \pm A/2| \qquad (1)$$

From the line splitting the hfc A can directly be obtained. In frozen solution the ENDOR signals from each proton—or group of equivalent protons—are smeared out over the whole range of the anisotropic hf tensor, and tensor principal components can be obtained from the spectral features in the powder-type ENDOR spectrum (for details see refs *60* and *61*). Axially symmetric hyperfine coupling tensors of freely rotating methyl groups exhibiting a small hf anisotropy can, for example, easily be analyzed yielding the two principal values, A_{II} and $A_{\perp}$. Furthermore, exchangeable protons coupled to the radical can be discriminated by investigation of the quinone radical in deuterated solvents. Due to the smaller Zeeman frequency of ^{2}H, ENDOR lines of deuterons usually do not contribute to the ^{1}H ENDOR range.

Panels A and B of Figure 8 show the ^{1}H ENDOR spectra of $MQ_4^{-\bullet}$ at 123 K in protonated and deuterated 2-propanol. We observe several line pairs (labeled a,a′, b,b′, etc.), whose respective hyperfine splittings are summarized in Table 4. In the spectrum obtained in deuterated 2-propanol only ^{1}H ENDOR lines from nonexchangeable protons of the $MQ_4^{-\bullet}$ molecule remain; other lines, e.g., from protons in hydrogen bonds, which are replaced by deuterons, are missing.

The spectral shape of pattern i,i′ and h,h′ resembles that of an axially symmetric hyperfine tensor, as expected for protons of a freely rotating methyl group. We therefore assign these line pairs in Figure 8B to the A_{II} and $A_{\perp}$ component of the CH_3 protons at position 3 (10.1 and 6.6 MHz, respectively). The resulting isotropic value of 7.8 MHz is in fair agreement with the value for vitamin $K_1^{-\bullet}$ in liquid solution (7.3 MHz) that has a similar structure (*62*, *63*). The observed anisotropy $(A_{\mathrm{II}} - A_{\perp})/A_{\mathrm{iso}}$ is rather large for protons of a rotating methyl group. However, for anion radicals of other methyl-substituted quinone radical anions, similar values were found (*4*, *64*). The magnitude of the anisotropy can be explained by the additional effect of the large spin density of the adjacent carbonyl group on the dipolar hyperfine coupling of the methyl protons. Couplings c,c′ and e,e′ (1.5 and 3.0 MHz, respectively) in Figure 8B are assigned to the two methylene protons of the side chain at position 2 (Figure 1). The reduction of these coupling constants as compared with those of vitamin $K_1^{-\bullet}$ in liquid solution (3.7 MHz) (*62*, *63*) indicates a preferred out-of-plane conformation of the side chain in frozen solution. This leads to a larger dihedral angle for the CH_2 protons ($\theta = 60°$) as compared with $\theta_{\mathrm{av}} = 45°$ for a rotating CH_3 group. The β-proton hfcs are proptional to the π-spin density at the neigboring carbon atom, ρ_c^{π}, and to $\cos^2\theta$ according to (*65*)

$$A_{\mathrm{iso}}(\mathrm{H}_{\beta}) = \rho_c^{\pi}(B_0 + B_2 \cos^2\theta) \qquad (2)$$

in which B_0 is usually negligibly small. Therefore, the π spin densities at carbon positions 2 and 3 could be of comparable magnitude, even though the hfcs of their β-protons are different. A preferred out-of-plane conformation of the side chain has recently been reported to be present in several methyl-substituted quinones in frozen solution (*66*). The α-protons at positions 5−8 of the quinone (Figure 1) are expected to be small and are therefore assigned to couplings a,a′ and b,b′ and may contribute to some extent also to coupling c,c′.

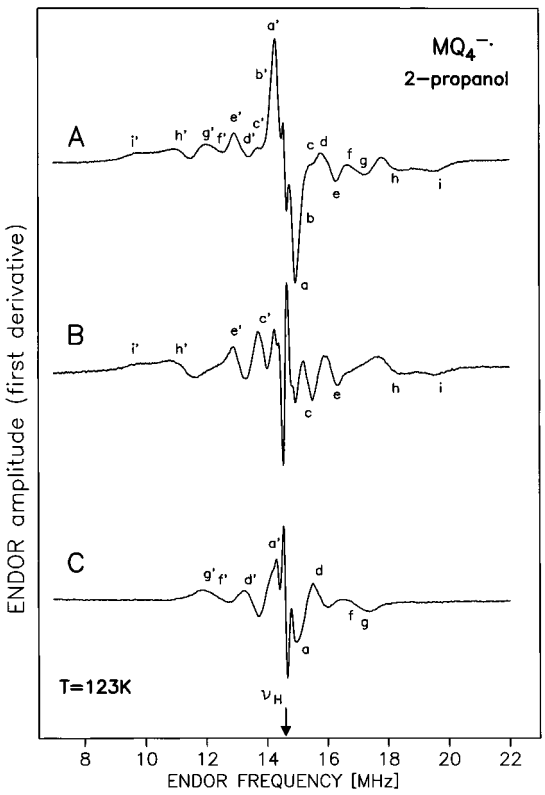

FIGURE 8: Powder-type cw ENDOR spectra (X-band) for $MQ_4^{-\bullet}$ in 2-propanol (A) and in fully deuterated 2-propanol-d_8 (B). In panel C the difference spectrum (A − B) is shown. The line pairs from which the hf splittings are obtained are marked (a,a′, b,b′, etc.); see Table 4. Note that in spectrum C only exchangeable protons from the surrounding medium contribute to the spectrum, e.g., protons involved in H bonds to the quinone oxygens. Experimental conditions: mw power 4 mW, accumulation time 80 min, rf power 150 W, 12.5 kHz FM, deviation ±25 kHz, and field setting, center of EPR line.

Table 4: Hyperfine Couplings for $MQ_4^{-\bullet}$ in 2-Propanol from ENDOR Spectroscopy

transition[a]	Hfc[b] (MHz)	assignments[c]
a,a′	0.5	α-proton and/or H-bond
b,b′	0.9	α-proton and/or H-bond
c,c′	1.5	CH_2 or α-proton
d,d′	2.2	H-bond $A_{\perp}$
e,e′	3.0	CH_2
f,f′	4.6	H-bond A_{II}
g,g′	5.5	H-bond A_{II}
h,h′	6.6	3-CH_3 ($A_{\perp}$)
i,i′	10.1	3-CH_3 (A_{II})

[a] For labeling of transitions, see spectra in Figure 8. [b] Errors ±0.1 MHz. [c] See Figure 1 for molecular structure and numbering of MQ_4.

In Figure 8C the difference between the spectra obtained in protonated and deuterated sovent is shown. Here, one observes only hf interactions resulting from exchangeable protons from the surrounding solvent. Similar spectra have been obtained for quinones with other substituents, e.g., plastoquinone-9, ubiquinone-10, and duroquinone anion radicals (*62*, *64*, *67*, *68*). The hfcs assigned to exchangeable protons (a,a′, d,d′, f,f′, and g,g′) are also given in Table 4. Their assignment is not immediately obvious. The two broad features giving rise to hf splittings f,f′ and g,g′ are assigned to $A_{||}$ components of two large hf tensors belonging to protons that are probably involved in hydrogen bonds to oxygens 1 and 4. The respective $A_{\perp}$ components arise either both from lines d,d′ or one from d,d′ and the other from a,a′, whereby the latter assignment is unlikely, since it leads to a rather large positive isotropic hf coupling of one H-bond proton.

On the basis of a comparison with literature values for other semiquinones (*64*), we assign couplings d,d′ (−2.2 MHz) and f,f′ (+4.6 MHz) to an exchangeable proton with a purely dipolar tensor ($A_{||}' = +4.6$, $A_{\perp}' = -2.3$, $A_{iso} \approx 0.1$ MHz). This proton most probably lies in the quinone plane. An $A_{\perp}$ component belonging to $A_{||} = +5.5$ MHz cannot be determined with confidence. It is probably overlapping with d,d′. We therefore assume that this second tensor is somewhat larger than the first one. We assign the two detected exchangeable protons to be hydrogen bonded to each of the carbonyl oxygens at position 1 and 4. We are unable to show, however, which is bound to which oxygen. The length of the first H bond estimated from the point-dipole approximation:

$$A'(\theta) = \frac{c}{r^3}\rho(3\cos^2\theta - 1) \qquad (3)$$

with $c = 79$ MHz Å^3 and a spin density on the oxygen estimated from ^{17}O hf data (*64*, *69*) of $\rho = 0.20$ gives $r_{OH} = 1.9$ Å. The second bond is expected to be somewhat shorter due to the larger $A_{||}$ value. The line pair a,a′ (Figure 8C) belonging to the hfc of an exchangeable proton is assigned to a hydrogen in a second solvation shell of the quinone.

The point-dipole approximation is not very reliable for short distances and distributed spin densities. More reliable results are obtained from DFT calculations performed on H-bonded quinone anion radicals (*59*, *70*, *71*), which yield both dipolar and isotropic hfcs for all nuclei for a certain geometry. For the naphthoquinone anion radical H-bonded in plane by methanol molecules ($r_{OH} \approx 1.8$ Å), dipolar tensor components of +5.8, −2.8, and −3.1 MHz ($A_{iso} = +0.2$ MHz) are calculated (*59*). This tensor is somewhat larger than the one obtained for $MQ_4^{-\bullet}$ in our experiments, indicating that for $MQ_4^{-\bullet}$ the H-bonds are somewhat longer. Increased values are calculated for out-of-plane H-bonding (*59*). Due to the substitution pattern of $MQ_4^{-\bullet}$, such a situation is likely to occur for this radical and the second larger H-bond tensor found in our experiments could be assigned to an out-of-plane H-bond.

ENDOR of $Q_A^{-\bullet}$ in ZnRCs of Rps. viridis. The ENDOR spectra obtained for $Q_A^{-\bullet}$ in ZnRCs from *Rps. viridis* are shown in Figure 9. The values for the hyperfine couplings are summarized in Table 5. In the spectrum recorded in deuterated buffer (Figure 9B) only the hf splittings from the nonexchangeable protons attached to the quinone and the protein matrix are detected. Since it is difficult to distinguish between ENDOR lines from methyl and side-chain methylene protons at positions 3 and 2, respectively, we base our assignment on the comparison with $MQ_4^{-\bullet}$ in frozen alcoholic solution (Figure 8). The largest splitting i,i′ (8.5 MHz) is assigned to the $A_{||}$ component of the hyperfine tensor of methyl protons at position 3. Since for this position a similar hyperfine anisotropy can be expected as for $MQ_4^{-\bullet}$ in vitro, we assign the corresponding $A_{\perp}$ component to splitting h,h′ (6.0 MHz). The resulting isotropic part A_{iso} is 6.8 MHz.

Splittings g,g′ and e,e′ (5.0 and 3.5 MHz, respectively) are then assigned to the two methylene β-protons of the side chain. From the X-ray structure, dihedral angles θ of −60° and +57° are obtained for the two methylene β-protons for the neutral Q_A molecule. This shows that the side chain is oriented perpendicular to the quinone plane and the two methylene protons should have similar hfcs. Line pair g,g′ is assigned to the $A_{||}$ and e,e′ to the $A_{\perp}$ component of their

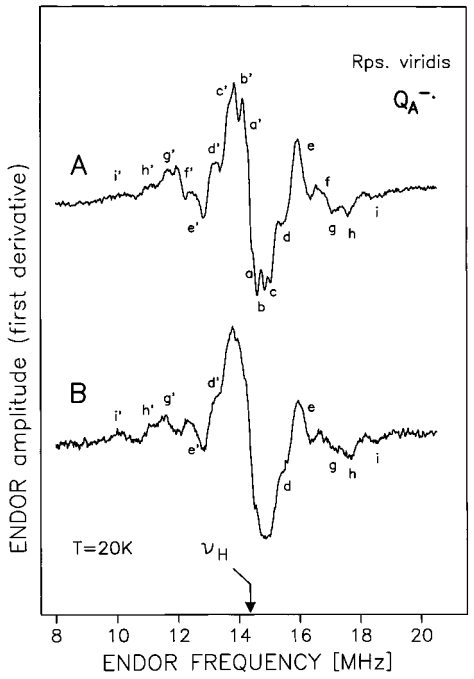

FIGURE 9: Powder-type cw ENDOR spectra (X-band) of $Q_A^{-\bullet}$ in ZnRCs of *Rps. viridis*. Line pairs from which the hf splittings are obtained are marked (a,a′, b,b′, etc.); see Table 5. (A) H_2O buffer, (B) D_2O buffer. Experimental conditions: mw power 4 mW, rf power 150 W, 12.5 kHz FM, deviation ±200 kHz, accumulation time 240 min, and field setting, center of EPR line.

Table 5: Hyperfine Couplings for $Q_A^{-\bullet}$ in ZnRCs of *Rps. viridis* from ENDOR Spectroscopy

transition[a]	Hfc[b] (MHz)	assignments[c]
a,a′	0.3	α-protons or matrix
b,b′	0.9	α-protons or matrix
c,c′	1.3	α-protons or matrix
d,d′	2.0	α-protons or matrix
e,e′	3.5	2-CH_2
f,f′	4.6	H-bond ($A_{\perp}$)
g,g′	5.0	2-CH_2
h,h′	6.0	3-CH_3 ($A_{\perp}$)
i,i′	8.5	3-CH_3 ($A_{||}$)

[a] For labeling of transitions, see spectra in Figure 9. [b] Error ±0.2 MHz. [c] See Figure 1 for molecular structures and numbering of menaquinone.

hyperfine tensor. Alternatively, the two hf splittings could be assigned each to one proton of the CH_2 group. Dihedral angles of $-65°$ and $+55°$ would be sufficient to produce the observed difference in hfcs (see eq 2). It should be noted in this context that the side-chain orientation of Q_A in *Rps. viridis* is quite different from that of Q_A in *Rb. sphaeroides*. In the latter case dihedral angles of $+38°$ and $-82°$ are obtained from the X-ray structure (*6*). The corresponding $\cos^2\theta$ values are 0.62 and 0.02. Consequently a large coupling from only *one* methylene β-proton has been observed for $Q_A^{-\bullet}$ in RCs of *Rb. sphaeroides*; the other one must be very small (*4*).

Comparison of the hyperfine values of $Q_A^{-\bullet}$ in the RC and $MQ_4^{-\bullet}$ in alcoholic solution (Tables 4 and 5) shows that the methyl proton hfc (A_{iso}) is significantly smaller in the RC, whereas the methylene proton hyperfine splittings are increased. The spin density at position 3, which is sensed by the methyl proton coupling, is reduced by 13% in $Q_A^{-\bullet}$ as compared with $MQ_4^{-\bullet}$ in vitro. Assuming a similar out-of-plane orientation of the methylene side chain for $MQ_4^{-\bullet}$ *in vitro* (*66*) as for $Q_A^{-\bullet}$ in *Rps. viridis*, it can be deduced from eq 2 that the spin density of position 2 is significantly increased in $Q_A^{-\bullet}$. Since in eq 2 $\cos^2\theta = 0.5$ for a rotating methyl group, and $\cos^2\theta = 0.25$ for $\theta = 60°$, assumed for the CH_2 group, the data indicate that in $Q_A^{-\bullet}$ the spin density at carbon 2 is larger than at carbon 3. This finding is very similar to the situation found for $UQ_{10}^{-\bullet}$ in vitro and $Q_A^{-\bullet}$ in the RC of *Rb. sphaeroides* (*4*).

The observed shift of spin density can be understood by postulating a different environment of the two carbonyl groups. One intriguing possibility is the formation of a stronger hydrogen bond to the proximal carbonyl (O_4) group and a weaker hydrogen bond to the distal carbonyl (O_1) of the $Q_A^{-\bullet}$ radical. The resulting effect on the spin density distribution can be explained on the basis of a simple valence bond picture (see refs *4* and *16*) and is also found in DFT calculations with asymmetric H-bonding to quinone radical anions (*71*, *72*). This asymmetric H-bond situation leads to an increase of spin density on carbon 2 but a decrease of the spin density on carbon 3. Hence, we observe a smaller hfc for the methyl group at position 3 in the $Q_A^{-\bullet}$ spectrum in the RC as in the corresponding spectrum of $MQ_4^{-\bullet}$ in frozen alcoholic solution, in which the H bonds are probably weaker and more symmetric (see above). Other interactions with the environment, e.g., with the divalent metal ion, could also contribute to the observed spin density shifts in $Q_A^{-\bullet}$ (*72*).

Due to the low signal-to-noise ratio a reliable ENDOR difference spectrum of $Q_A^{-\bullet}$ in protonated and deuterated buffer (Figure 9, A−B) could not be obtained. It is, however, obvious from Figure 9A that at least one additional line pair (f,f′) is observed in H_2O that disappears if D_2O buffer is used. This is particularly pronounced on the low-frequency side of the spectrum as expected for a H-bond interaction resulting form a dipolar tensor (see refs *13* and *14*). A second pronounced line pair is not clearly observed in the spectra. On the basis of its line shape and magnitude we assign splitting f,f′ of 4.6 MHz (Table 5) to the $A_\perp$ component of a proton in a hydrogen bond between the protein and one carbonyl oxygen of $Q_A^{-\bullet}$. This value is larger than that observed for $MQ_4^{-\bullet}$ and other quinone anion radicals in vitro in alcoholic solvents (*62*, *64*), indicating the presence of a fairly strong hydrogen bond. From the direction of the shift of spin densities at ring positions 2 and 3 detected in the ^1H ENDOR spectra, it is concluded that this strong H bond is formed to O_4 (Figure 1); i.e., to the less sterically hindered carbonyl group of Q_A.

The existence of a second H bond in *Rps. viridis* cannot be excluded at present from the available ENDOR data; it must, however, be of different strength as compared to the first one. An indication for a second H bond comes from the above-described observation of two ^{14}N nuclear quadrupole coupling constants that are assigned to nitrogens from a histidine and a peptide backbone. Two hydrogen bonds to the carbonyl groups have also been clearly identified for $Q_A^{-\bullet}$ in ZnRCs of *Rb. sphaeroides* (*4*).

Comparison with Crystallographic Data. In Figure 6 the structure of the Q_A site in *Rps. viridis* is shown. In the ground-state X-ray crystallographic study two H bonds between the protein and Q_A are indicated (*5*). In this recent structural refinement a shorter distance has been found between O_4 of Q_A and the $N^{\delta(1)}$ of His(M217) (2.9 Å) than between O_1 of Q_A and the backbone nitrogen of Ala(M258) (3.1 Å). This is in qualitative agreement with our spectroscopic data. It has been shown by X-ray crystallography of RC single crystals of *Rb. sphaeroides* in the ground state and the charge-separated state $P^+Q_A^{-\bullet}$ (*73*) that no significant change in structure and position of $Q_A^{-\bullet}$ as compared with Q_A occurs.

Experiments on the Radical Pair State $P_{960}^{+\bullet}Q_A^{-\bullet}$ in ZnRCs

Transient EPR Experiments of $P_{960}^{+\bullet}Q_A^{-\bullet}$. As shown in a number of transient EPR studies, information about the relative orientation of the two cofactors involved in a radical pair (RP) can be deduced from simulations of the transient EPR spectra, based on the CCRP (correlated coupled radical pair) model as reviewed in refs *20*, *74* and *75*. To get a reliable set of orientational parameters, measurements of the RP spectra in various frequency bands are required.

A characteristic X-band electron spin polarization (ESP) pattern with E/A/E (E = emission, A = enhanced absorption) is well-established for ZnRCs of *Rb. sphaeroides* (*76*) and can be attributed to the RP state $P_{865}^{+\bullet}Q_A^{-\bullet}$. Similar experiments with *Rps. viridis* are more complicated due to the bound cytochrome *c* subunit. The redox potentials of the four hemes have been measured (*77*, *78*) and have the following sequence: P_{960}, heme 3, heme 4, heme 2, heme 1. Without addition of oxidants or reductants, hemes 4, 2, and 1 are oxidized but heme 3 is only partially (~50%) oxidized (G. Fritzsch, personal communication). Upon laser excitation, in a fraction of the RCs, the primary donor $P_{960}^{+\bullet}$ will be reduced by the nonoxidized heme 3 fraction within 250 ns, which is much faster than the recombination of the RP state $P_{960}^{+\bullet}Q_A^{-\bullet}$ (approximately 1.5 ms). As a result, after reduction of $P_{960}^{+\bullet}$ this fraction of the sample contains prereduced $Q_A^{-\bullet}$, which blocks ET past the bacteriopheophytin (BPh). Further light excitation of this RC fraction results in the formation of the intermediary RP state $P_{960}^{+\bullet}BPh^{-\bullet}$, followed by charge recombination to the triplet state of the primary donor, $^3P_{960}$ (*79*). The observation of the RP signal of $P_{960}^{+\bullet}Q_A^{-\bullet}$ alone is therefore not possible in *Rps. viridis* since the heme 3 cannot be fully oxidized without oxidizing part of P_{960}.

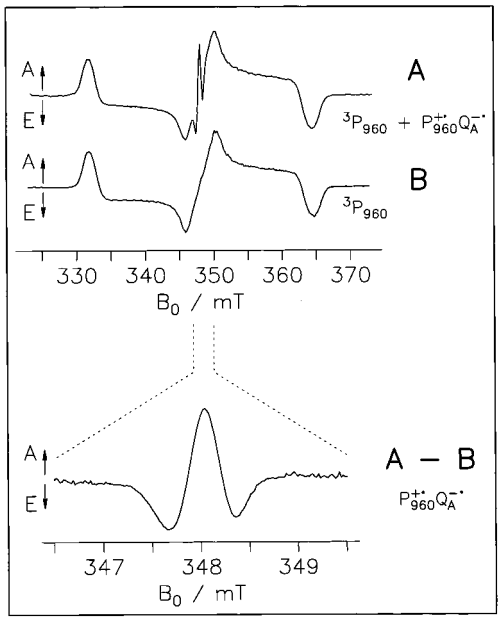

FIGURE 10: (A) Superposition of the $^3P_{960}$ signal and the RP spectrum of $P_{960}^+ \bullet Q_A^- \bullet$ in ZnRCs of *Rps. viridis* in a sample with no oxidant or reductant added. (B) Spectrum of $^3P_{960}$ in an FeRCs *Rps. viridis* sample. The bottom spectrum shows the difference between A and B in the $g = 2$ region on an expanded scale, showing the pure RP spectrum of $P_{960}^+ \bullet Q_A^- \bullet$. All spectra have been measured at X-band at $T = 100$ K. The transient EPR signals were integrated in the time gate 0.5−2.0 μs after the laser flash; mw power 220 μW, accumulation time 20 min.

Figure 10A shows the transient X-band EPR spectrum of *Rps. viridis* recorded at 100 K. It can be attributed to a superposition of a triplet signal and the RP signal of $P_{960}^+ \bullet Q_A^- \bullet$. From the triplet spectrum, the D and E values of $|D| = 162.0 \pm 1.5$ cm^{-1} and $|E| = 41.0 \pm 1.5$ cm^{-1} are obtained, which are in good agreement with values reported in the literature for $^3P_{960}$ (see ref *80* and references therein). The observed polarization pattern (A/E/E/A/A/E) can be explained as a result of selective population of the $|T_0\rangle$ sublevel due to the recombination of the intermediary radical pair $P_{960}^+ \bullet BPh^- \bullet$ (*79*). Oxidation of heme 3 by FeCy results in a drastic decrease of the $^3P_{960}$ intensity (see below). Therefore, we can conclude that the $^3P_{960}$ state observed here is due to centers in which heme 3 reduced $P_{960}^+ \bullet$ in the charge-separated state $P_{960}^+ \bullet [Fe^{2+}Q_A^- \bullet]$, i.e., in centers containing Q_A. It should be noted that at a temperature of 100 K, the A/E/E/A/A/E polarization pattern for $^3P_{960}$ is also observed for Fe-containing (native) RCs (Figure 10B). This is in contrast to previous work (*30*, *81*, *82*) in which a different polarization pattern has been reported for native Q_A-containing RCs of *Rps. viridis*. The reason for the observed differences remains to be clarified.

For an analysis of the RP spectrum, a subtraction of the triplet spectrum is necessary. The spectrum of $^3P_{960}$ without the superimposed RP can be measured under the same conditions in native Fe^{2+}-containing samples as shown in Figure 10B. The difference spectrum is depicted in Figure 10, bottom (A−B), for the region near $g = 2$. It shows an E/A/E polarization pattern similar to that obtained for *Rb. sphaeroides* R-26 (*83*). However, the RP spectrum of $P_{960}^+ \bullet Q_A^- \bullet$ shows a smaller spectral width than that of $P_{865}^+ \bullet Q_A^- \bullet$, consistent with the smaller g anisotropy of $Q_A^- \bullet$ in *Rp. viridis* as compared with $Q_A^- \bullet$ in *Rb. sphaeroides*. The relative intensities of the two emissive peaks are changed in comparison with *Rb. sphaeroides* R-26 (*83*).

Due to the low amount of Zn substitution (∼50%, see above), transient EPR signals, arising from the RP $P_{960}^+ \bullet [Fe^{2+}$-$Q_A^- \bullet]$ in RCs that still contain the non-heme iron, can disturb the observed spectrum for $P_{960}^+ \bullet Q_A^- \bullet$ in the ZnRCs. The spin-polarized EPR spectrum of $P_{960}^+ \bullet [Fe^{2+}Q_A^- \bullet]$ shows an A/E/A polarization pattern (*30*) similar to the one observed in native RCs of *Rb. sphaeroides* R-26 (*84*, *85*). However, the contribution of this signal to the observed spectrum shown in Figure 10A is expected to be very small at a temperature of 100 K. For native RCs of *Rb. sphaeroides* R-26, a strong increase of the relaxation of the spin polarization of $P_{865}^+ \bullet [Fe^{2+}Q_A^- \bullet]$ is observed at increasing temperature, followed by a drastic decrease of its signal intensity (*86*). Although the signal of $P_{865}^+ \bullet [Fe^{2+}Q_A^- \bullet]$ is visible up to ∼200 K without a change in polarization at early times, the intensity reduces by about a factor of 5 from 6 to 100 K. Thus, the intensity of $P_{865}^+ \bullet [Fe^{2+}Q_A^- \bullet]$ is at least one order of magnitude smaller than for $P_{865}^+ \bullet Q_A^- \bullet$. In analogy to these results, the contribution of $P_{960}^+ \bullet [Fe^{2+}Q_A^- \bullet]$ to the transient spectra discussed here has been neglected. This is in accordance with the spectrum of the native sample (Figure 10B) where no additional signal in the $g \approx 2$ region, which could be ascribed to $P_{960}^+ \bullet [Fe^{2+}Q_A^- \bullet]$, is observed.

For a detailed discussion of the geometrical arrangement of the two cofactors, a measurement of the RP signal at various frequency bands is necessary, since the relative influence of the hyperfine coupling on the spectra decreases with increasing microwave (mw) frequency. Furthermore, at higher mw frequencies the spectum is better resolved as the g anisotropy becomes dominant. On the other hand, since the spectrum is spread out over a wider range, the absolute intensity per Gauss tends to decrease at higher mw frequencies. Therefore, for a measurement of the RP spectrum at Q-band, the triplet background has to be suppressed as much as possible. For this purpose, we added an 80-fold excess of FeCy to the sample (see the Materials and Methods section). This led to a decrease of the triplet backgrond by a factor of 5 but decreased the intensity of the RP signal only slightly (≤10%). Further addition of FeCy resulted in oxidation of P_{960}, monitored by the optical absorption band at 960 nm, and a drastical decrease of the RP signal intensity (data not shown).

Figure 11A shows the transient Q-band EPR spectra of $P_{960}^+ \bullet Q_A^- \bullet$ in the FeCy-treated sample after subtraction of the small remaining triplet background. For comparison, the RP spectra of $P_{865}^+ \bullet Q_A^- \bullet$ of *Rb. sphaeroides* R-26 is depicted in Figure 11B. Both spectra show a similar polarization pattern (A/E/A/E/A). The low-field A/E/A part of the $P_{960}^+ \bullet Q_A^- \bullet$ spectrum is shifted to slightly higher fields compared with $P_{865}^+ \bullet Q_A^- \bullet$, corroborating the smaller spectral width already found at X-band. From the similar polarization pattern in the low-field part of the spectra a similar orientation of the quinones in both RCs is deduced. The Q-band spectra can be simulated by using the orientational parameter obtained from the X-ray structures of *Rps. viridis* (*5*) and *Rb. sphaeroides* R-26 (*6*, *87*), respectively. The simulations are shown in Figure 11 by dotted lines. The simulation is satisfactory for the quinone part of the spectrum (low-field), while in the P part (high-field) some differences between experiment and simulation are evident. Mainly two

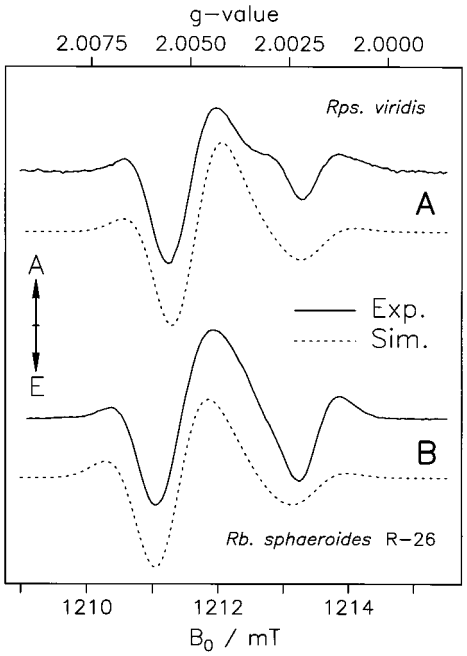

FIGURE 11: Transient EPR spectra of *Rps. viridis* (A) and *Rb. sphaeroides* R-26 (B) measured at Q-band at $T = 100$ K. Integration window 1.5−5.0 μs after the laser flash; mw power 133 μW. Simulations with the cofactor arrangement obtained from X-ray structures (*5*, *87*) are shown as dotted lines. Simulation parameters (*Rps. viridis*): $g(P^{+}\bullet)$, 2.00309, 2.00251, 2.00205 (*88*); $g(Q_A^{-}\bullet)$, see Table 2; line widths, $\Delta B(P^{+}\bullet) = 1$ mT, $\Delta B(Q_A^{-}\bullet) = 0.7$ mT; Euler angles, $\alpha = 19°$, $\beta = 119°$, $\gamma = 14°$, $\theta = 72°$, $\varphi = 68°$ (**g** tensor orientation taken from ref *89*); spin−spin coupling, $D = -116$ μT, $J = 1$ μT. The parameters used for the simulation of the *Rb. sphaeroides* spectrum are given in ref *90*.

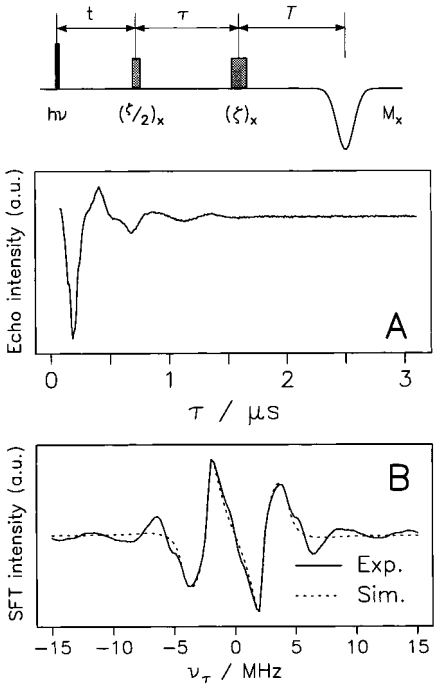

FIGURE 12: (A) Two-pulse ESEEM time traces for the RP $P_{960}^{+}\bullet Q_A^{-}\bullet$ in *Rps. viridis* ZnRCs at $T = 150$ K. (B) Sine Fourier transforms of the experimental ESEEM traces after dead-time reconstruction (—) and numerical simulations (- - -). The data evaluation and parameters obtained from the simulations are discussed in the text. Top: pulse sequence used for the experiment.

reasons are responsible for the observed differences: (i) the orientation of the **g**-tensor of $P_{960}^{+}\bullet$ with respect to the molecular axes system has not yet been determined, and (ii) anisotropic hfcs may contribute to the spectrum. These are not included in our simulation because of the large number of unknown parameters (principal values and directions of each hfc tensor). However, from a comparison of the numerical simulation based on the ground-state X-ray structure with the experimental spectrum, we conclude that no detectable reorientation of $Q_A^{-}\bullet$ occurs as a result of the Zn substitution procedure. This is in agreement with the results found for *Rb. sphaeroides* R-26 (*90*).

Pulsed EPR Experiments of $P_{960}^{+}\bullet Q_A^{-}\bullet$. Additional information on the RC structure can be obtained from the determination of the cofactor distance between $P_{960}^{+}\bullet$ and $Q_A^{-}\bullet$. This distance can be derived from a pulsed electron spin echo (ESE) experiment performed on the RP state. A two-pulse ESE experiment gives rise to an out-of-phase echo showing a deep envelope modulation (ESEEM) as a function of the pulse spacing. The modulation frequency of the ESEEM is dominated by the interaction between the two electron spins within the RP, which consists of the isotropic coupling J and the dipolar coupling D. Both can be evaluated from the simulation of the Fourier tranformed echo modulation (see, e.g, refs *28*, *91*). Since the dipolar coupling shows a simple distance dependence with $D = -2786$ mT/r^3, it is possible to derive the distance r between the two RP spins located on the cofactors $P_{960}^{+}\bullet$ and $Q_A^{-}\bullet$ and compare it with the distance found for the cofactors in the ground state by X-ray crystallography.

It should be noted that the ESEEM experiment on a spin-correlated light-induced RP is substantially different from the similar experiment on a stablilized single radical. ESEEM experiments on a single radical are able to yield small electron−nuclear hyperfine couplings and quadrupole interactions as described above. The echo modulation frequency in an ESEEM experiment on the RP state is the same in protonated and deuterated (*28*) as well as in ^{14}N or ^{15}N-enriched samples (*91*). For this reason, contributions from hyperfine and quadrupole interactions can be neglected in these experiments and the spectra are only dominated by the electron−electron interaction.

Figure 12A shows the out-of-phase echo modulation of $P_{960}^{+}\bullet Q_A^{-}\bullet$ in ZnRCs of *Rps. viridis* measured at 150 K. The ESEEM is similar to that of $P_{865}^{+}\bullet Q_A^{-}\bullet$ in ZnRCs of *Rb. sphaeroides* R-26 (*28*). In particular, the modulation frequency deviates only slightly, indicating that the distances between the spins in both RCs are very similar. Detailed information on the cofactor distance can be achieved, e.g., by a comparison between the Fourier transform of the experimental ESEEM after reconstruction of the signal within the spectrometer deadtime and its numerical simulation according to the CCRP model mentioned above. In Figure 12B the sine Fourier transform (SFT) of the experimental out-of-phase echo modulation is shown together with the numerical simulation. For the upper limit of isotropic coupling J, a value of $J \leq 1.0$ μT, consistent with the simulation of the transient EPR spectra (*92*), has been derived for *both* RCs. From the numerical simulation we obtained a dipolar coupling of $D = -(116 \pm 4)$ μT for *Rps. viridis*. From this value, a distance of 28.8 ± 0.3 Å between the centers of the spin densities on $P_{960}^{+}\bullet$ and $Q_A^{-}\bullet$ in *Rps. viridis* is calculated. The distance obtained for ZnRCs of

Rb. sphaeroides in a similar experiment was 28.4 ± 0.3 Å (*28*). From the X-ray structure of *Rps. viridis* (*5*) a cofactor distance[3] of 28.3 ± 0.4 Å between $P_{960}^{+\bullet}$ and $Q_A^{-\bullet}$ is derived, assuming that the spin on $P_{960}^{+\bullet}$ is located mainly on the L half of the dimer[4] and the spin on $Q_A^{-\bullet}$ is located in the center between the carbonyl oxygens. This distance is in reasonable agreement with the distance between the RP spins measured in our pulsed EPR experiment.

SUMMARY AND CONCLUSION

In reaction centers of *Rps. viridis* the non-heme high-spin Fe^{2+} has been partially replaced by Zn^{2+}. The resulting RCs have been purified and characterized by biochemical and spectroscopic methods. This includes time-resolved optical measurements to determine the electron-transfer kinetics as well as cw, transient and pulsed EPR techniques to obtain the **g** tensor and hyperfine couplings of the primary quinone acceptor radical anion, $Q_A^{-\bullet}$, as well as structural parameters from the radical pair $P_{960}^{+\bullet}Q_A^{-\bullet}$. The data have been compared with those obtained earlier from ZnRCs of *Rb. sphaeroides*.

The analysis of the transient EPR spectra of the radical pair states $P^+Q_A^{-\bullet}$ in both *Rps. viridis* and *Rb. sphaeroides* showed that the relative orientation of these radicals is very similar. It also agrees with the available X-ray crystallographic structure (*5*, *6*, *87*) in the ground state. This indicates that no *major* reorientation of the cofactors takes place during charge separation (cf. also ref *73*). The distance between the spins in the radical pairs was determined from out-of-phase ESEEM experiments. It is the same within experimental error for both bacterial RCs, in agreement with the X-ray crystallographic structures.

The **g**-tensor of $Q_A^{-\bullet}$ in *Rps. viridis* RCs measured by Q-band EPR characterizes this species as a naphthoquinone-type radical anion. The shifts of the **g** tensor components—in particular of g_x—with respect to a model compound in alcoholic solution is similar to that observed for ubiquinone in the A-site of *Rb. sphaeroides* ZnRCs (*40*). It seems to be characteristic for the specific binding sites of Q_A in the protein.

The proton hyperfine coupling constants of $Q_A^{-\bullet}$ determined by cw ENDOR spectroscopy clearly show a shift of spin density in the quinone ring as compared with the menaquinone radical anion in alcoholic solution. This effect is qualitatively identical to that found for $Q_A^{-\bullet}$ in *Rb. sphaeroides* (*4*, *14*). Furthermore, D_2O exchange experiments identified at least one exchangeable proton in $Q_A^{-\bullet}$ that could be assigned to a hydrogen bond between a carbonyl group of $Q_A^{-\bullet}$ and the protein. The magnitude of the observed coupling indicates a fairly strong H-bond. A second H-bond could not be clearly resolved in the spectra. The shift of spin density in the quinone ring is attributed mainly to asymmetric H-bonding of the two C−O groups of $Q_A^{-\bullet}$. On the basis of a valence bond model (*4*), the stronger bond should be to the oxygen O_4 adjacent to the CH_3 group of the menaquinone; i.e., to the less sterically hindered carbonyl group. This finding is in agreement with data obtained for $Q_A^{-\bullet}$ in *Rb. sphaeroides* from EPR/ENDOR on selectively isotope-labeled systems (*15*, *16*) and FTIR (*43*, *44*) techniques. A similar situation was also found for menaquinone in *Rps. viridis* RCs by FTIR (*93*, *94*).

Support for a second H-bond comes from our ESEEM data that show interaction of the semiquinone anion radical $Q_A^{-\bullet}$ with two nitrogens from the surrounding protein. A comparison of the respective ^{14}N nuclear quadrupole coupling constants with those of various amino acid residues indicates that one nitrogen most probably belongs to a $N^{\delta(1)}$−H of histidine and one to an N−H of the protein backbone. Two different H-bonds to the C−O groups of $Q_A^{-\bullet}$ in *Rb. sphaeroides* have been found experimentally by following the intensity change of the respective ENDOR signals during D_2O exchange (*4*, *95*). A recent X-ray structure analysis of *Rps. viridis* RCs (*5*) shows that the carbonyl oxygens of Q_A are within H-bond distance to His(M217) and Ala(M258). A very similar situation is found for the Q_A site in *Rb. sphaeroides* RCs (*6*, *87*).

Obviously, Nature has used the same basic concept to form the peculiar Q_A binding site in both bacterial species to achieve the specific function of this electron carrier. It is postulated that the binding site described here will also be found in other photosynthetic bacteria and in photosystem II of plant photosynthesis that perform similar functions.

ACKNOWLEDGMENT

We are grateful to I. Geisenheimer (TU Berlin) for her help with the preparation and to G. Fritzsch and R. Lancaster (both Max-Planck-Institut für Biophysik, Frankfurt Main) for providing coordinates of *Rps. viridis* RCs, for preparing Figure 9, and for helpful discussions concerning the Q_A binding site. E. C. Abresch (UC San Diego) performed the AAS measurements on the ZnRC samples, which is gratefully acknowledged.

REFERENCES

1. Deisenhofer, J., and Michel, H. (1989) *EMBO J. 8*, 2149−2170.
2. Feher, G., Allen, J. P., Okamura, M. Y., and Rees, D. C. (1989) *Nature 339*, 111−116.
3. Okamura, M. Y., and Feher, G. (1995) in *Anoxygenic Photosynthetic Bacteria* (Blankenship, R. E., Madigan, M. T., and Bauer, C. E., Eds.) pp 577−594, Kluwer Academic Publishers, Dordrecht, The Netherlands.
4. Lubitz, W., and Feher, G. (1999) *Appl. Magn. Reson. 17*, 1−48.
5. Lancaster, R. C. D., and Michel, H. (1997) *Structure 5*, 1339−1359.
6. Stowell, M. H. B., McPhillips, T. M., Rees, D. C., Soltis, S. M., Abresch, E., and Feher, G. (1997) *Science 276*, 812−816.
7. Butler, W. F., Calvo, R., Fredkin, D. R., Isaacson, R. A., Okamura, M. Y., and Feher, G. (1984) *Biophys. J. 45*, 947−973.
8. Gast, P., Gottschalk, A., Norris, J. R., and Closs, G. L. (1989) *FEBS Lett. 243*, 1−4.
9. Evelo, R. G., Nan, H. M., and Hoff, A. J. (1988) *FEBS Lett. 239*, 351−357.
10. Feher, G., and Okamura, M. (1999) *Appl. Magn. Reson. 16*, 63−100.

[3] Considering the coordinate error of the X-ray structural data for each atom (0.3 Å) (*5*), the error for the $P_{865}^{+\bullet} \Leftrightarrow Q_A^{-\bullet}$ distance can be estimated to be at least 0.4 Å.

[4] It is assumed that the spin is predominantly on the BChl *b* dimer half bound to the L protein subunit in analogy to the dimer in RCs of *Rb. sphaeroides*. For a localization of the spin on the M half, a distance of 28.0 ± 0.4 Å is obtained; for a symmetric spin distribution in the dimer, a distance of 27.9 ± 0.4 Å is found (center between the two dimer halves).

11. Debus, R. J., Feher, G., and Okamura, M. Y. (1986) *Biochemistry 25*, 2276−2287.
12. Burghaus, O., Plato, M., Rohrer, M., Möbius, K., MacMillan, F., and Lubitz, W. (1993) *J. Phys. Chem. 97*, 7639−7647.
13. Lubitz, W., Abresch, E. C., Debus, R. J., Isaacson, R. A., Okamura, M. Y., and Feher, G. (1985) *Biochim. Biophys. Acta 808*, 464−469.
14. Feher, G., Isaacson, R. A., Okamura, M. Y., and Lubitz, W. (1985) *Springer Series in Chemical Physics*, Vol. 42, pp 174−189, Springer-Verlag, Berlin.
15. van den Brink, J. S., Spoyalov, A. P., Gast, P., van Liemt, W. B. S., Raap, J., Lugtenburg, J., and Hoff, A. J. (1994) *FEBS Lett. 353*, 273−276.
16. Isaacson, R. A., Abresch, E. C., Lendzian, F., Boullais, C., Paddock, M. L., Mioskowski, C., Lubitz, W., and Feher, G. (1996) in *The Reaction Center of Photosynthetic Bacteria—Structure and Dynamics* (Michel-Beyerle, M.-E., Ed.) pp 353−367, Springer-Verlag, Berlin.
17. Bosch, M. K., Gast, P., Hoff, A. J., Spoyalov, A. P., and Tsvetkov, Y. D. (1995) *Chem. Phys. Lett. 239*, 306−312.
18. Lendzian, F., Rautter, J., Käss, H., Gardiner, A., and Lubitz, W. (1996) *Ber. Bunsen-Ges. Phys. Chem. 100*, 2036−2040.
19. Spoyalov, A. P., Hulsebosch, R. J., Shochat, S., Gast, P., and Hoff, A. J. (1996) *Chem. Phys. Lett. 263*, 715−720.
20. Stehlik, D., and Möbius, K. (1997) *Annu. Rev. Phys. Chem.* 48, 745−784.
21. Zech, S. G., Bittl, R., Gardiner, A. T., and Lubitz, W. (1997) *Appl. Magn. Reson. 13*, 517−529.
22. Borovykh, I. V., Dzuba, S. A., Proskuryakov, I. I., Gast, P., and Hoff, A. J. (1998) *Biochim. Biophys. Acta 1363*, 182−186.
23. Gardiner, A. T., Lendzian, F., MacMillan, F., Zech, S. G., Bittl, R., Kuhn, M., and Lubitz, W. (1995) in *Photosynthesis: From Light to Biosphere* (Mathis, P., Ed.) Vol. I, pp 655−658, Kluwer Academic Publishers, Dordrecht, The Netherlands).
24. Thornber, J. P., Seftor, R. E. B., and Cogdell, R. J. (1981) *FEBS Lett. 134*, 235−239.
25. Rieger, P. H. (1982) *J. Magn. Reson. 50*, 485−489.
26. Press, W. H., Teukolsky, S. A., Vetterling, W. T. and Flannery, B. P. (1992) *Numerical Recipes in C: The Art of Scientific Computing*, 2nd ed., Cambridge University Press, Cambridge, England.
27. Bittl, R., Zech, S. G., and Lubitz, W. (1996) in *The Reaction Center of Photosynthetic Bacteria—Structure and Dynamics* (Michel-Beyerle, M.-E., Ed.) pp 333−339, Springer-Verlag, Berlin.
28. Bittl, R., and Zech, S. G. (1997) *J. Phys. Chem. B 101*, 1429−1436.
29. Bittl, R., van der Est, A., Kamlowski, A., Lubitz, W. and Stehlik, D. (1994) *Chem. Phys. Lett. 226*, 349−358.
30. van den Brink, J. S., Hermolle, T. E. P., Gast, P., Hore, P. J., and Hoff, A. J. (1996) *J. Phys. Chem. 100*, 2430−2437.
31. Käss, H., Rautter, J., Bönigk, B., Höfer, P., and Lubitz, W. (1995) *J. Phys. Chem. 99*, 436−448.
32. Käss, H., Rautter, J., Zweygart, W., Struck, A., Scheer, H., and Lubitz, W. (1994) *J. Phys. Chem. 98*, 354−363.
33. Rautter, J., Lendzian, F., Lubitz, W., Wang, S., and Allen, J. P. (1994) *Biochemistry 33*, 12077−12084.
34. Zweygart, W., Thanner, R., and Lubitz, W. (1994) *J. Magn. Reson. A109*, 172−176.
35. Sebban, P., and Wraight, C. A. (1989) *Biochim. Biophys. Acta 974*, 54−65.
36. Gao, J.-L., Shopes, R. J., and Wraight, C. (1991) *Biochim. Biophys. Acta 1056*, 259−272.
37. Kirmaier, C., Holten, D., Debus, R. J., Feher, G., and Okamura, M. Y. (1986) *Proc. Natl. Acad. Sci. U.S.A. 83*, 6407−6411.
38. Schelvis, J. P. M., Liu, B.-L., Aartsma, T. J., and Hoff, A. J. (1992) *Biochim. Biophys. Acta 1102*, 229−236.
39. Debus, R. J., Feher, G., and Okamura, M. Y. (1985) *Biochemistry 24*, 2488−2500.
40. Isaacson, R. A., Lendzian, F., Abresch, E. C., Lubitz, W., and Feher, G. (1995) *Biophys. J. 69*, 311−322.
41. Nimz, O., Lendzian, F., Boullais, C., and Lubitz, W. (1998) *Appl. Magn. Reson. 14*, 255−274.
42. Hoff, A. J., Kropacheva, T. N., Samoilova, R. I., Gritzan, N. P., Raap, J, van den Brink, J.S., Gast, P., and Lugtenburg, J. (1996) in *The Reaction Center of Photosynthetic Bacteria—Structure and Dynamics* (Michel-Beyerle, M. E., Ed.) pp 405−420, Springer-Verlag, Berlin.
43. Breton, J., Boullais, C., Burie, J.-R., Nabedryk, E., and Mioskowski, C. (1994) *Biochemistry 33*, 14378−14386.
44. Brudler, R., deGroot, H. J. M., van Liemt, W. B. S., Steggerda, W. F., Esmeijer, R., Gast, P., Hoff, A. J., Lugtemburg, J., and Gerwert, K. (1994) *EMBO J. 13*, 5523−5530.
45. Deisenhofer, J., Epp, O., Miki, K., Huber, R., and Michel, H. (1985) *Nature 318*, 618−624.
46. Eshouf, R. M. (1997) *J. Med. Graphics 15*, 133−138.
47. Kraulis, P. J. (1991) *J. Appl. Crystallogr. 24*, 946−950.
48. Dikanov, S. A., and Tsvetkov, Y. D. (1992) *Electron Spin Echo Envelope Modulation (ESEEM) Spectroscopy*, CRC Press, Boca Raton, FL.
49. Käss, H., Bittersmann-Weidlich, E., Andréasson, L.-E., Bönigk, B., and Lubitz, W. (1995) *Chem. Phys. 194*, 419−432.
50. Flanagan, H., and Single, D. J. (1987) *J. Chem. Phys. 87*, 5606.
51. Deligiannakis, Y., Jegerschold, C., and Rutherford, A. W. (1997) *Chem. Phys. Lett. 270*, 564−572.
52. Creighton, T. E. (1993) *Proteins, Structures and Molecular Properties*, 2nd ed., W. H. Freeman and Co., New York.
53. Edmonds, D. T., and Summers, C. D. (1973) *J. Magn. Reson. 12*, 134−142.
54. Blinc, R., Moli, M., Osredkar, R., and Seliger, J. (1974) *Chem. Phys. Lett. 28*, 158−159.
55. Deligiannakis, Y., Boussac, A., and Rutherford, A. W. (1995) *Biochemistry 34*, 16030.
56. Astashkin, A. V., Kawamori, A., Kodera, Y., Kuroiwa, S., and Akabori, K. (1995) *J. Chem. Phys. 102*, 5583−5588.
57. MacMillan, F., Kurreck, J., Adir, N., Lendzian, F., Käss, H., Reifarth, F., Renger, G., and Lubitz, W. (1995) in *Photosynthesis: from Light to Biosphere* (Mathis, P., Ed.) Vol. I, pp 659−662, Kluwer Academic Publishers, Dordrecht, The Netherlands.
58. Peloquin, J. M., Tang, X.-S., Diner, B. A., and Britt, R. D. (1999) *Biochemistry 38*, 2057−2067.
59. O'Malley, P. J. (1999) *Biochim. Biophys. Acta 1411*, 101−113.
60. Kurreck, H., Kirste, B., and Lubitz, W. (1988) in *Methods in Stereochemical Analysis* (Marchand, A. P., Ed.) VCH Publishers, Inc., Deerfield Beach, FL.
61. Lubitz, W., and Lendzian, F. (1996) in *Biophysical Techniques in Photosynthesis* (Amesz, J., and Hoff, A. J., Eds.) pp 255−275, Kluwer Academic Publishers, Dordrecht, The Netherlands.
62. MacMillan, F. (1993) Doctoral Thesis, Freie Universität Berlin, Germany.
63. Das, M. R., Connor, H. D., Leniart, D. S., and Freed, J. H. (1970) *J. Am. Chem. Soc. 92*, 2258−2268.
64. MacMillan, F., Lendzian, F., and Lubitz, W. (1995) *Magn. Reson. Chem. 33*, 81−93.
65. Atherton, N. (1993) *Principles of Electron Spin Resonance* pp 104−108, Ellis Horwood, New York.
66. Zheng, M., and Dismukes, G. C. (1996) *Biochemistry, 35*, 8955−8963.
67. MacMillan, F., Lendzian, F., Renger, G., and Lubitz, W. (1995) *Biochemistry 34*, 8144−8156.
68. Rohrer, M., Plato, M., MacMillan, F., Grishin, Y., Lubitz, W., and Möbius, K. (1995) *J. Magn. Reson. A116*, 59−66.
69. Pedersen, J. A. (1985) *Handbook of EPR Spectra from Quinones and Quinols*, CRC Press, Boca Raton, FL.
70. O'Malley, P. J. (1997) *J. Phys. Chem. A, 101*, 9813−9817.
71. O'Malley, P. J. (1998) *J. Phys. Chem. A, 102*, 248−253.
72. O'Malley, P. J. (1998) *Chem. Phys. Lett. 285*, 99−104.
73. Abresch, A. C., Yeh, A. P., Soltis, S. M., Rees, D. C., Axelrod, H. L., Okamura, M. Y., and Feher, G. (1999), *Biophys. J.* 76, A141 (abstract M-AM-D6).
74. Angerhofer, A., and Bittl, R. (1996) *Photochem. Photobiol. 63*, 11−38.

75. van der Est, A., and Stehlik, D. (1996) in *The Reaction Center of Photosynthetic Bacteria—Structure and Dynamics* (Michel-Beyerle, M.-E., Ed.) pp 321−332, Springer-Verlag, Berlin.
76. Snyder, S. W., and Thurnauer, M. C. (1993) in *The Photosynthetic Reaction Center* (Deisenhofer, J., and Norris, J. R., Eds.) Vol. II, pp 285−330, Academic Press, San Diego, CA.
77. Fritzsch, G., Buchanan, S., and Michel, H. (1989) *Biochim. Biophys. Acta 977*, 157−162.
78. Nitschke, W., and Rutherford, A. W. (1989) *Biochemistry 28*, 3161−3168.
79. Budil, D. E., and Thurnauer, M. C. (1991) *Biochim. Biophys. Acta 1057*, 1−41.
80. Angerhofer, A. (1991) in *Chlorophylls* (Scheer, H., Ed.) pp 945−991, CRC Press, Boca Raton, FL.
81. van Wijk, F. G. H., Gast, P., and Schaaftsma, T. J. (1986) *Photochem. Photophys. 11*, 95−100.
82. van Wijk, F. G. H., Gast, P., and Schaaftsma, T. J. (1986) *FEBS Lett. 206*, 238−241.
83. Füchsle, G., Bittl, R., van der Est, A., Lubitz, W., and Stehlik, D. (1993) *Biochim. Biophys. Acta 1142*, 23−35.
84. Proskurjakov, I. I., Klenina, I. B., Shkuropatov, A. Y. Shkuropatova, V. A., and Shuvalov, V. A. (1993) *Biochim. Biophys. Acta 1142*, 203−210.
85. Snyder, S. W., Morris, A. L., Bouderon, S. R., Norris, J. R., and Thurnauer, M. C. (1993) *J. Am. Chem. Soc. 115*, 3774−3775.
86. Zech, S. G., Gardiner, A. T., Lubitz, W., and Bittl, R. (1998) in *Magnetic Resonance and Related Phenomena* (Ziessow, D., Lubitz, W., and Lendzian, F., Eds.) pp 949−950, Technische Universität Berlin, Berlin, Germany.
87. Ermler, U., Fritzsch, G., Buchanan, S. K., and Michel, H. (1994) *Structure 2*, 925−936.
88. Törring, J. (1996) Doctoral Thesis, Freie Universität Berlin, Germany.
89. Klette, R., Törring, J. T., Plato, M., Möbius, K. Bönigk, B., and Lubitz, W. (1993) *J. Phys. Chem., 97*, 2015−2020.
90. Prisner, T. F., van der Est, A., Bittl, R., Lubitz, W., Stehlik, D., and Möbius, K. (1995) *Chem. Phys. 194*, 361−370.
91. Dzuba, S. A., Gast, P., and Hoff, A. J. (1995) *Chem. Phys. Lett. 236*, 595−602.
92. van den Brink, J. S., Hulsebosch, R. J., Gast, P., Hore, P. J., and Hoff, A. J. (1994) *Biochemistry 33*, 13668−13677.
93. Breton, J., and Nabedryk, E. (1996) *Biochim. Biophys. Acta 1275*, 84−90.
94. Breton, J. (1997) *Proc. Natl. Acad. Sci. U.S.A. 94*, 11318−11323.
95. Paddock, M. L., Abresch, E. C., Isaacson, R. A., Lubitz, W., Okamura, M. Y., and Feher, G. (1999) *Biophys. J. 76*, A141 (abstract M-AM-D7).

BI990661C